

Conformal piezoelectric energy harvesting and storage from motions of the heart, lung, and diaphragm

Canan Dagdeviren^{a,1}, Byung Duk Yang^{a,1}, Yewang Su^{b,c,1}, Phat L. Tran^d, Pauline Joe^a, Eric Anderson^a, Jing Xia^{b,c}, Vijay Doraiswamy^d, Behrooz Dehdashti^e, Xue Feng^f, Bingwei Lu^b, Robert Poston^e, Zain Khalpey^e, Roozbeh Ghaffari^g, Yonggang Huang^c, Marvin J. Slepian^{d,h}, and John A. Rogers^{a,i,2}

^aDepartment of Materials Science and Engineering, Beckman Institute for Advanced Science and Technology, and Frederick Seitz Materials Research Laboratory, and ^bDepartments of Chemistry, Mechanical Science and Engineering, and Electrical and Computer Engineering, University of Illinois at Urbana-Champaign, Urbana, IL 61801; ^cCenter for Mechanics and Materials and ^dDepartment of Engineering Mechanics, Tsinghua University, Beijing 100084, China; ^eDepartment of Civil and Environmental Engineering, Department of Mechanical Engineering, Center for Engineering and Health, and Skin Disease Research Center, Northwestern University, Evanston, IL 60208; ^fDepartment of Medicine and Sarver Heart Center and Departments of ^gSurgery and ^hBiomedical Engineering, The University of Arizona, Tucson, AZ 85724; and ⁱMC10 Inc., Cambridge, MA 02140

Edited by Joseph M. DeSimone, The University of North Carolina at Chapel Hill, Chapel Hill, NC, and approved December 16, 2013 (received for review September 12, 2013)

Here, we report advanced materials and devices that enable high-efficiency mechanical-to-electrical energy conversion from the natural contractile and relaxation motions of the heart, lung, and diaphragm, demonstrated in several different animal models, each of which has organs with sizes that approach human scales. A cointegrated collection of such energy-harvesting elements with rectifiers and microbatteries provides an entire flexible system, capable of viable integration with the beating heart via medical sutures and operation with efficiencies of ~2%. Additional experiments, computational models, and results in multilayer configurations capture the key behaviors, illuminate essential design aspects, and offer sufficient power outputs for operation of pacemakers, with or without battery assist.

biomedical implants | flexible electronics | transfer printing | wearable electronics | heterogeneous integration

Nearly all classes of active wearable and implantable biomedical devices rely on some form of battery power for operation. Heart rate monitors, pacemakers, implantable cardioverter-defibrillators, and neural stimulators together represent a broad subset of bioelectronic devices that provide continuous diagnostics and therapy in this mode. Although advances in battery technology have led to substantial reductions in overall sizes and increases in storage capacities, operational lifetimes remain limited, rarely exceeding a few days for wearable devices and a few years for implants. Surgical procedures to replace the depleted batteries of implantable devices are thus essential, exposing patients to health risks, heightened morbidity, and even potential mortality. The health burden and costs are substantial, and thus motivate efforts to eliminate batteries altogether, or to extend their lifetimes in a significant way.

Investigations into energy-harvesting strategies to replace batteries demonstrate several unusual ways to extract power from chemical, mechanical, electrical, and thermal processes in the human body (1, 2). Examples include use of glucose oxidation (3), electric potentials of the inner ear (4), mechanical movements of limbs, and natural vibrations of internal organs (5–7). Such phenomena provide promising opportunities for power supply to wearable and implantable devices (6–8). A recent example involves a hybrid kinetic device integrated with the heart for applications with pacemakers (7). More speculative approaches, based on analytical models of harvesting from pressure-driven deformations of an artery by magneto-hydrodynamics, also exist (9).

Cardiac and lung motions, in particular, serve as inexhaustible sources of energy during the lifespan of a patient. Mechanical-to-electrical transduction mechanisms in piezoelectric materials offer viable routes to energy harvesting in such cases, as demonstrated and analyzed by several groups recently (10–17). For example, proposals exist for devices that convert heartbeat vibrations into electrical energy using resonantly coupled motions of

thick (1–2 mm) piezoelectric ceramic beams on brass substrates (1). Although such models highlight the potential for self-powering devices, there are important practical challenges in the coupling of rigid mechanical systems with the soft, dynamic surfaces of the body in a manner that does not induce adverse side effects. An ideal device construct would enable power harvesting throughout the macroscale displacement cycles associated with natural motions of an organ, but in a manner that does not induce any significant constraints on those motions. Development of flexible devices based on arrays of piezoelectric ZnO nanowires (14, 15) represents an important step in this direction. Experiments performed with a linear motor to periodically deform the device indicate electrical outputs as large as 1–2 V (open-circuit voltage) and ~100 nA (short-circuit current) (13). Initial *in vivo* tests on rabbit hearts yielded voltages and currents of ~1 mV and ~1 pA, respectively. The associated electrical power is substantially less than that required for operation of existing classes of implants, such as pacemakers. Some improvement in performance is possible with thin-film geometries, as demonstrated in bending experiments on devices based on barium titanate (16) and lead zirconate titanate (PZT) (11, 12, 17). *In vivo* evaluations are needed, however, to assess the suitability for realistic use and potential for producing practical levels of power.

Significance

Heart rate monitors, pacemakers, cardioverter-defibrillators, and neural stimulators constitute broad classes of electronic implants that rely on battery power for operation. Means for harvesting power directly from natural processes of the body represent attractive alternatives for these and future types of biomedical devices. Here we demonstrate a complete, flexible, and integrated system that is capable of harvesting and storing energy from the natural contractile and relaxation motions of the heart, lung, and diaphragm at levels that meet requirements for practical applications. Systematic experimental evaluations in large animal models and quantitatively accurate computational models reveal the fundamental modes of operation and establish routes for further improvements.

Author contributions: C.D., B.D.Y., P.L.T., M.J.S., and J.A.R. designed research; C.D., P.L.T., P.J., E.A., V.D., B.D., X.F., B.L., R.P., Z.K., M.J.S., and J.A.R. performed research; C.D., Y.S., J.X., V.D., B.D., R.P., Z.K., Y.H., M.J.S., and J.A.R. contributed new reagents/analytic tools; C.D., Y.S., P.L.T., P.J., Y.H., M.J.S., and J.A.R. analyzed data; and C.D., Y.S., P.L.T., R.G., Y.H., M.J.S., and J.A.R. wrote the paper.

The authors declare no conflict of interest.

This article is a PNAS Direct Submission.

¹C.D., B.D.Y., and Y.S. contributed equally to this work.

²To whom correspondence should be addressed. E-mail: jrogers@illinois.edu.

This article contains supporting information online at www.pnas.org/lookup/suppl/doi:10.1073/pnas.1317233111/-DCSupplemental.

The present work reports several advances in the materials science and engineering of biocompatible, flexible, energy harvesters. The key findings include *in vivo* demonstrations of PZT-based devices (*i*) with output open-circuit voltages and short-circuit currents that are greater by three and five orders of magnitude, respectively, than previous *in vivo* results; (*ii*) monolithically integrated with rectifiers and millimeter-scale batteries for simultaneous power generation and storage, including high-power, multilayer designs; (*iii*) in biocompatible forms, evaluated through cell cultures and large-scale, live animal models, on various locations/orientations on different internal organs, each approaching human scales; and (*iv*) for harvesting inside the body, via open and closed left thoracotomy experiments with a bovine model. Additional results demonstrate (*i*) power generation at a level necessary for continuous operation of a cardiac pacemaker; (*ii*) mechanically and electrically stable device behavior over 20 million cycles of bending/unbending in a moist, hydrogel environment; and (*iii*) quantitatively accurate analytical models that couple mechanical deformations and piezoelectric effects to predict electrical output as a function of key design parameters and materials properties, including multilayer configurations.

Results and Discussion

Fig. 1A and *SI Appendix, Figs. S1 and S2* provide schematic diagrams of a flexible PZT mechanical energy harvester (MEH). An optical microscope image and a photograph appear in Fig. 1B and C, respectively. The key functional element is a capacitor-type structure that consists of a layer of PZT (500 nm) between bottom (Ti/Pt, 20 nm/300 nm) and top (Cr/Au, 10 nm/200 nm) electrodes. See *SI Appendix* for details. An MEH module consists of 12 groups of 10 such structures that are electrically connected in parallel. Each of the 12 groups is connected in series to its neighboring group to increase the output voltage (*SI Appendix, Fig. S2*). Encapsulation of these devices with biocompatible materials isolates them from bodily fluids and tissue, thereby minimizing the risks of failure or immune response. A thin spin-cast layer of polyimide (PI) (*SI Appendix*) serves effectively in this role, as demonstrated in leakage tests performed in PBS (P-5368, pH 7.4; SIGMA) in a way that maintains excellent mechanical flexibility. The computed bending stiffness (per unit width) is 0.22 N-mm and 0.10 N-mm for regions coincident with and away from the PZT structures, respectively. For a bending radius of 2.5 cm, the maximum strain in the PZT is only 0.1%.

As a screen of the biocompatibility and absence of cytotoxicity of the constituent materials, we examined the adherence, growth, and viability of rat smooth muscle cells (SMCs), as a representative tissue cell, on the encapsulated PZT capacitor structures described above. SMCs readily adhere to fibronectin-coated structures, with evident spreading (Fig. 1D), and intact detectable cytoskeletal structures, i.e., Vinculin focal contacts via fluorescence (green in Fig. 1D) and cytoskeletal actin microfilaments (red in Fig. 1E). The scanning electron microscope (SEM) image shows spreading cells in Fig. 1F. No detectable cytotoxicity was observed in a live/dead assay that identifies calcein acetomethoxy derivative (green) for viable cells and ethidium homodimer (red) for damaged cells, suggesting that the majority of SMCs are healthy (green in Fig. 1D). In fact, more than 96% of cells were viable after 9 d of culture. Cells grown on device structures showed no differences from those grown on standard tissue culture plates at days 3 and 9 (Fig. 1G).

Measurements with a bending stage reveal dynamic mechanical properties, as shown in Fig. 2A. Fig. 2B illustrates 3D deformations of the PZT ribbons, with distributions of strain obtained by finite element analysis (FEA). The overall shapes match those observed in Fig. 2A. The strain distributions in *SI Appendix, Figs. S3 and S4* quantitatively capture the nature of deformations in the various device layers. The results determine the electrical field and electrical displacement in the PZT through constitutive models of piezoelectric behavior. The voltage and current outputs of a representative device before (Fig. 2C)

and after (*SI Appendix, Fig. S5*) rectification illustrate the nature of operation. See *SI Appendix* for details.

Experimental behaviors can be captured with an analytical model. Compression of a device with length L leads to buckling with an out-of-plane displacement $w = A[1 + \cos(2\pi x_1/L)]/2$ as shown in *SI Appendix, Fig. S6A*, where the origin of coordinate x_1 is at the center of the device, and the amplitude A is related to the compression ΔL between the two ends by $A \approx (2/\pi)\sqrt{L \cdot \Delta L}$. The PZT layers, together with the top and bottom electrodes, bend with the buckled substrate. The membrane strain in the PZT ribbons is given analytically by

$$\varepsilon_m = 4\pi \frac{\overline{EI}_{PI}}{\overline{EI}_{comp}} \frac{h}{L} \sqrt{\frac{\Delta L}{L}}, \quad [1]$$

(see *SI Appendix* for details), where \overline{EI}_{comp} and \overline{EI}_{PI} are the bending stiffness (per unit width) of the PI with and without the PZT and electrodes, respectively; and h is the distance from the center of the PZT layers to the neutral mechanical plane of the cross-section as shown in *SI Appendix, Fig. S6B*. The bending strain in the PZT ribbons has opposite signs above and below the

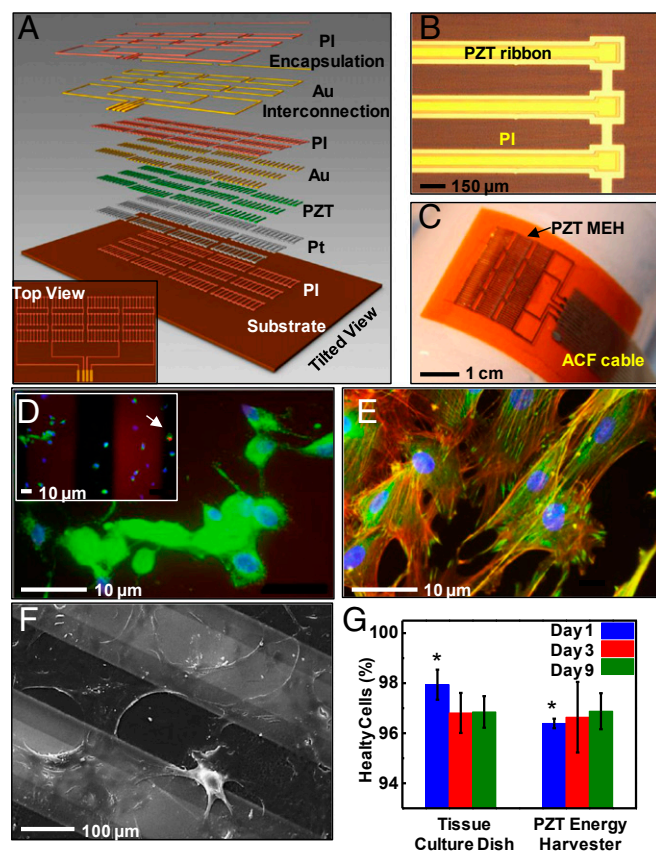


Fig. 1. Flexible MEH based on thin ribbons of PZT, and tests of biocompatibility using rat smooth muscle cells. (A) Exploded-view schematic illustration with a top view (*Inset*). (B) Optical microscope image of PZT ribbons printed onto a thin film of PI. (C) Photograph of a flexible PZT MEH with cable for external connection. ACF, anisotropic conductive film. (D) Live/dead viability assay showing live cells (green) with intact nucleus (blue) and one dead cell (red) as indicated by the arrow (*Inset*). This image corresponds to day 9 of the experiment. (E) Fluorescent image showing Vinculin focal contact points (green), actin filaments (red), and nuclei (blue). (F) SEM image of cells on PZT ribbons encapsulated by a layer of PI. (G) Lactate dehydrogenase assay shows no indications of toxicity for cells on a membrane of PZT at day 9. (* P value ≤ 0.05 between the two groups.) Error bar is calculated standard error.

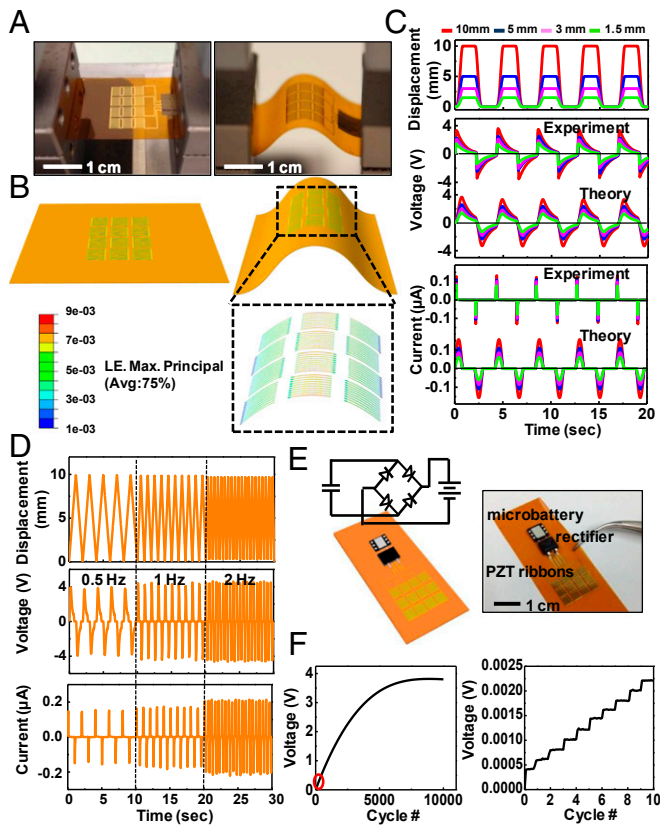


Fig. 2. Experimental and theoretical studies of the electrical behavior of PZT MEHs under various mechanical loads. (A) Photographs of a PZT MEH clamped on a bending stage in flat (Left) and bent (Right) configurations. (B) Three-dimensional finite element method modeling for the device in A. The results highlighted by the black dashed box give the computed distributions of strain in the PZT ribbons for a displacement load of 5 mm along the horizontal direction. LE, logarithmic strain. (C) Experimental and theoretical results for displacement, voltage, and current as a function of time for PZT MEHs under bending loads similar to those shown in A and B. (D) Displacement, voltage, and current as a function of time curves, for bending loads with frequencies of 0.5, 1, and 2 Hz. (E) Schematic illustration (Left) and photograph (Right) of a PZT MEH connected to and cointegrated with a rectifier and rechargeable microbattery. A circuit schematic appears in Left. (F) Voltage across such a battery as a function of time during charging by a PZT MEH under cyclic bending load (Left). The peak voltage output of the PZT MEH is 4.5 V. The red oval (Left) highlights, approximately, the region plotted (Right). The results highlight the expected stepwise behavior in charging.

midpoint through the thickness of the PZT, and therefore does not contribute to the voltage or current output. For thin PZT layers, the bending strain is much smaller than the membrane strain; the total strain is therefore dominated by the membrane strain. See *SI Appendix* for details.

PZT is transversely isotropic with the polarization direction x_3 normal to the surface. The elastic, piezoelectric, and dielectric constants are denoted by c_{ij} , e_{ij} , and k_{ij} , respectively. For plane-strain deformation ($\epsilon_{22} = 0$) the strain ϵ_{33} and the electrical field E_3 along the polarization direction x_3 satisfy the constitutive relations $0 = c_{11}\epsilon_{11} + c_{13}\epsilon_{33} - e_{31}E_3$ and $D_3 = e_{31}\epsilon_{11} + e_{33}\epsilon_{33} + k_{33}E_3$, where the electrical displacement D_3 along the polarization direction is a constant to be determined. For measurements of current, the top and bottom electrodes connect to an ammeter, which has negligible electrical resistance. As a result, voltage between the top and bottom electrodes is zero, and $D_3 = \bar{e}\epsilon_m$, where the effective piezoelectric constant is $\bar{e} = e_{31} - (c_{13}/c_{33})e_{33}$ and the membrane strain ϵ_m is given in Eq. 1. For each group of devices in

series, the charge induced by ϵ_m gives the current $I = -A_{PZT}\dot{D}_3$ (*SI Appendix*, Fig. S6C), i.e.,

$$I = (-\bar{e})A_{PZT}\frac{d\epsilon_m}{dt}, \quad [2]$$

where A_{PZT} is total area of the PZT ribbons in each group. In experiments, the compression ΔL between the two ends of the device is a periodic function of time t , given by

$$\Delta L = \begin{cases} \frac{\Delta L_{max}}{4} \left[1 - \cos\left(\frac{\pi t}{T_1}\right) \right]^2, & 0 \leq t < T_1 \\ \Delta L_{max}, & T_1 \leq t < T_1 + T_2 \\ \frac{\Delta L_{max}}{4} \left\{ 1 - \cos\left[\frac{\pi(t - 2T_1 - T_2)}{T_1}\right] \right\}^2, & T_1 + T_2 \leq t < 2T_1 + T_2 \\ 0, & 2T_1 + T_2 \leq t < 2(T_1 + T_2) \end{cases} \quad [3]$$

in the first period, where ΔL_{max} is the maximum compression, and $T = 2(T_1 + T_2)$ is the period. Fig. 2C shows ΔL vs. t for $T_1 = 0.8$ s, $T_2 = 1.3$ s, and $\Delta L_{max} = 1.5, 3, 5,$ and 10 mm as in the experiments. Fig. 2C shows that the current obtained from Eq. 2 for these four values of ΔL_{max} agree reasonably well with the experiments, where $L = 2.5$ cm, $EI_{PI}/EI_{comp} = 0.45$, $h = 24.7$ μ m, and $A_{PZT} = 2.24$ mm² as in the experiments (see *SI Appendix* for details), and $\bar{e} = -10$ Coulomb/m², which is on the same order of magnitude as the literature values (18). The peak current ranges from 0.06 to 0.15 μ A for ΔL_{max} from 1.5 to 10 mm, respectively.

In measurements of voltage, the potential drop across each group is V/N , where V is the total voltage for N groups of devices in series (*SI Appendix*, Fig. S6C). The electrical displacement is $D_3 = \bar{e}\epsilon_m + kV/(Nt_{PZT})$, where $k = k_{33} + (e_{33}^2/c_{33})$ is the effective dielectric constant and t_{PZT} is the thickness of PZT ribbons. The current $I = -A_{PZT}\dot{D}_3$ is related to the voltage V and resistance R of the voltmeter by $I = V/R$, which gives $V/R = -A_{PZT}\dot{D}_3$, i.e.,

$$\frac{dV}{dt} + \frac{Nt_{PZT}}{A_{PZT}Rk}V = -\frac{N\bar{e}t_{PZT}}{k}\frac{d\epsilon_m}{dt} \quad [4]$$

For the initial condition $V(t = 0) = 0$, the voltage is given by

$$V = \frac{(-\bar{e})Nt_{PZT}}{k} e^{-\frac{Nt_{PZT}}{A_{PZT}Rk}t} \int_0^t \frac{d\epsilon_m}{dt} e^{\frac{Nt_{PZT}}{A_{PZT}Rk}t} dt \quad [5]$$

For $R = 60 \times 10^6 \Omega$ in the experiment and $\bar{k} = 4 \times 10^{-8} C/Vm$ (18), Fig. 2C shows the voltage V vs. time t obtained from Eq. 5, which agrees well with the experiments, including both the shape and peak value. The peak voltage can reach values as large as 3.7 V for the maximum compression $\Delta L_{max} = 10$ mm. (The differences between the measured and predicted behavior of the output current in Fig. 2C arise because, according to Eqs. 1 and 2, the current is directly proportional to the rate of compression $d\Delta L/dt$, and is therefore sensitive to $d\Delta L/dt$ when the compression reverses direction. The assumed displacement profile does not follow precisely the one in the experiment. By contrast, the voltage is relatively insensitive to $d\Delta L/dt$ because Eqs. 1 and 5 involve the integration of $d\Delta L/dt$.)

Fig. 2D shows that the currents and voltages increase with frequency, even with the same load amplitudes, consistent with predicted dependence (Eqs. 2, 4 and 5) on the strain rate $d\epsilon_m/dt$. This behavior can be understood by recognizing that increasing the frequency with the same load amplitude increases the amount of work performed by the external force; as a result, the

harvester produces enhanced output energy through increases in current and voltage.

This energy can be captured directly by use of a chip-scale rechargeable battery (EnerChip CBC012; Cymbet Corporation) and a Schottky bridge rectifier (MB12S; Micro Commercial Components) cointegrated on the same flexible substrate with the MEHs. Characterization can be performed using the setups shown in Fig. 2A. Fig. 2E and F show the device and the output voltage of the battery measured in such a case; the results reveal stepwise increases in the stored energy with each cycle of bending and unbending (Fig. 2A). As the process continues, the voltage of the battery saturates at a value (~ 3.8 V) characteristic of the battery specification.

The analytical framework can be modified to account for the rectifier via its resistance $R_{rectifier}$, as illustrated in SI Appendix, Fig. S6D. Here, the resistance in the current measurement is $R_{rectifier}$ instead of 0, whereas the resistance R in the voltage measurement is replaced by $R + R_{rectifier}$. The voltage in Eq. 5 is replaced by its absolute value. See SI Appendix for details. The results (SI Appendix, Fig. S5) agree well with experiments. The amplitudes of the current and voltage are only slightly smaller than those without the rectifier.

An effective efficiency for conversion of mechanical energy to electrical energy can be defined as the ratio of energy stored in the battery W_{stored} to the total mechanical work W_{total} , i.e., $\eta = (W_{stored}/W_{total}) \times 100\%$. Here W_{stored} is estimated from the saturated voltage 3.8 V and capacity of the battery as 0.164 J. The total mechanical work is the product of the number of cycles for the battery voltage to saturate (e.g., 7,500 from Fig. 2F for $\Delta L_{max} = 10$ mm) and work done (19) in each cycle $\int_0^{\Delta L_{max}} F d\Delta L$, where $F = 4\pi^2 w_{PI} E I_{PI} / L^2$ is the bucking force (SI Appendix, Fig. S6A), and $w_{PI} = 2$ cm is the width. These calculations indicate an efficiency, at the system level, of $\eta = 1.7\%$. This value can be improved by decreasing the thicknesses and Young's moduli of the electrodes and PI encapsulation layer and/or by increasing the area coverage of the PZT. Reductions in viscoelastic dissipation of the substrate can also be helpful (19). [We note that alternative metrics for efficiency (13) lead to much higher values than those reported above.]

Additional in vitro characterization illustrates that these MEH devices can be wrapped onto various curved objects such as balloons, fingers, and wrists, as seen in SI Appendix, Fig. S7. Control experiments (SI Appendix, Fig. S8) reveal that reversing the electrical connections to measurement equipment reverses the signal polarity, as expected. The devices exhibit excellent fatigue properties. Bending and releasing more than 20 million times while in direct contact with a transparent layer of gelatin (Knox), to mimic a moist environment (SI Appendix, Fig. S9A and B), induce no noticeable degradation in the properties, as in SI Appendix, Fig. S9C and D.

In vivo testing involved affixing the devices to epicardial sites on the right ventricle (RV), left ventricle (LV) base, and free wall of bovine and ovine hearts as shown in Fig. 3A and Movies S1 and S2. The anchoring scheme used sutures at three points, to maintain focal contact, although without rigid attachment so as to minimize any alteration or constraint on cardiac motion. Similar suturing techniques have been previously used to suture 3D patches onto the LV in a rat model (20). Furthermore, alternative suturing techniques, including running locked stitch and five-point lacerations can further reinforce the attachments. No detectable change in cardiac conduction or epicardial motion occurs following this simple procedure for fixing the device onto the epicardium. The PZT MEH maintains conformal contact, without delamination from the heart during the entire cycle of cardiac motion from contraction to relaxation. Evaluation of various mounting sites can identify locations for optimal power extraction (Fig. 3A and B). Analysis of voltage outputs from devices placed on the RV, LV base, and free wall appear in Fig. 3C, D, and E, respectively. The RV yields the best results, even though the LV has more muscular fibers (9–11 mm thick) than the RV (3–5 mm thick) (21). The differences in shape and other functional characteristics are, however, most important. The RV chamber is box- or wedge-shaped in form, with a concave free wall, which is thinner than the LV and is attached to the convex interventricular septum (22). The LV is roughly cylindrical in shape and has a thick wall structure with three spiraling layers of muscle to enable contractions with a twisting or torsional motion (23, 24). The RV ejects blood primarily by shortening its free

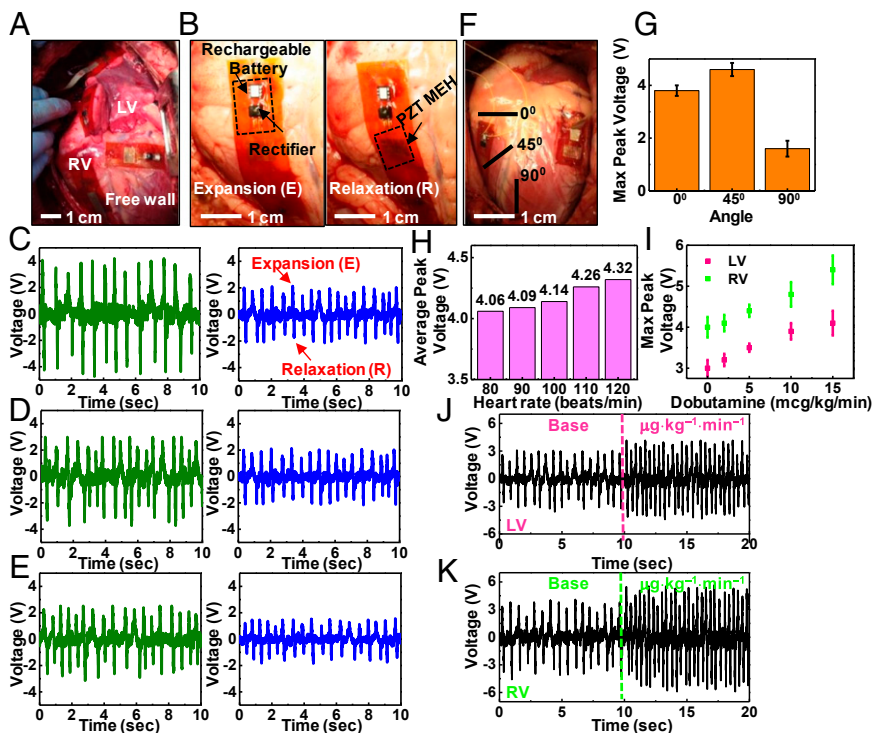


Fig. 3. In vivo evaluation of the optimal placement and orientation of PZT MEHs on the heart, and assessment of voltage output by varying the heart rate via dobutamine infusion and use of a temporary pacemaker. (A) Photograph of PZT MEHs on the RV, LV, and free wall of a bovine heart. (B) PZT MEH cointegrated with a rectifier and rechargeable battery, mounted on the RV of a bovine heart, shown during expansion (Left) and relaxation (Right). Open circuit voltage as a function of time for PZT MEHs on bovine (green) and ovine (blue) hearts, mounted on (C) RV, (D) LV, and (E) free wall at an orientation of 0° relative to the apex of the heart. Here, the heart rate is 80 beats per min. (F) Photograph of PZT MEHs oriented at different angles. (G) Measurements of maximum values of the peak open circuit voltages produced by these devices indicate peak output at 45°. Error bar is calculated standard error. (H) Average peak voltages of a PZT MEH on the RV of a bovine heart at 0° for various heart rates (80–120 beats per min) controlled by a temporary pacemaker. (I) Maximum peak voltage for various dosages of dobutamine infusion, for the case of a device on the RV (green points) and LV (pink points) of a bovine heart at 0°. Error bar is calculated standard error. Voltage as a function of time for PZT MEHs on the LV (J) and RV (K) of a bovine heart, with a base and maximum dose of dobutamine.

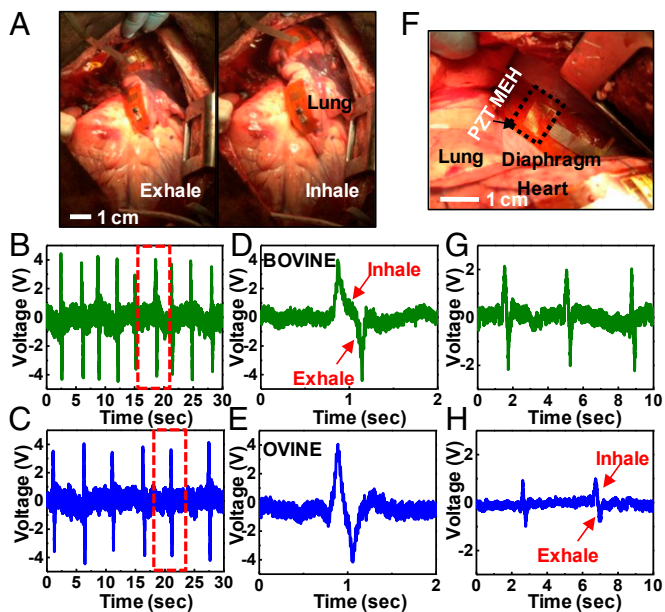


Fig. 4. In vivo evaluation of PZT MEHs on the lung and diaphragm. (A) Photograph of a PZT MEH cointegrated with a microbattery and rectifier, mounted on the bovine lung. Voltage as a function of time for such devices on the bovine (B) and ovine (C) lung. D and E show plots corresponding to the regions indicated by the red dashed boxes in B and C, respectively. (F) Photograph of a PZT MEH on the bovine diaphragm. Voltage as a function of time for such a device on the bovine (G) and ovine (H) diaphragm.

wall, whereas ejection from the LV primarily involves a reduction in its diameter or circumference, associated with wall thickening (25). The contraction of the RV by shortening the free wall likely results in enhanced overall wall motion and hence increased bending of the MEH than the twisting contraction of the LV.

Orientation of the device is also important, as illustrated by the data in Fig. 3 F and G. Bending in the longitudinal direction (x_1 direction in *SI Appendix*, Fig. S3) relative to the orientation of the PZT ribbons provides the highest efficiency (see *SI Appendix* for details). To examine the dependence on orientation on the heart, measurements involve the longitudinal direction of PZT ribbons along the 0° , 45° , and 90° directions with respect to the apex of the heart. The 0° and 45° directions produce greater voltages than those at 90° (Fig. 3G). This behavior, for 0° and 45° , is expected because the myocardial tissue of the heart is anisotropic and contracts in a generally circumferential direction (26) with cardiac

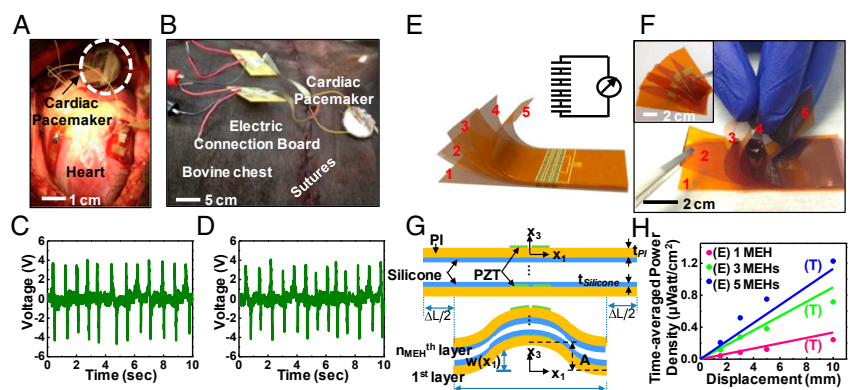
fibers aligned in a continuous manner from $+60^\circ$ on the endocardium to -60° on the epicardium (27); 90° is clearly out of this range. Theoretically, as shown in Eq. 5, the voltage is proportional to the strain rate, or equivalently, the strain amplitude for a given period. FEA confirms that the strain by bending along the x_1 direction is larger than that along x_2 , as shown in *SI Appendix*, Figs. S3 and S4. Aligning the x_1 direction with the strongest bending direction optimizes the harvested energy.

The size of the heart, beat rate, and force of contraction are additional factors that affect voltage output. In the studies reported here (Figs. 3–5), the bovine heart is nearly twice the mass of the ovine model. All devices deployed on the former yield significantly higher voltage outputs than those in the ovine model, for any site of implantation on the heart (*SI Appendix*, Figs. S10 and S11). Modulating the heart rate through electrical and chemical stimulation reveals the dependence on frequency. Fig. 3H demonstrates that increasing the bovine heart rate with a temporary pacemaker (Medtronic 5388) increases the voltage in direct proportion to heart rate (see *SI Appendix*, Figs. S10 and S11 and Movie S3), consistent with modeling results, assuming that the amplitude does not vary significantly with frequency. Similarly, increasing the force and degree of contractility of the myocardium via dobutamine infusion, i.e., the inotropic state ($15 \mu\text{g}\cdot\text{kg}^{-1}\cdot\text{min}^{-1}$), increases both the voltage and the frequency of the output (*SI Appendix*, Fig. S12). Such a response occurs for both the LV and RV, as shown in Fig. 3 I–K.

The lung represents another internal organ of interest for mechanical energy harvesting. Results for mounting on the bovine (Fig. 4A and Movie S4) and ovine lung of the bovine are consistent with expectation. In particular, in both models respiratory movement can be converted to voltage (Fig. 4 B and D). Unlike observations with the heart, data collected from the lung show no strong interspecies differences (Fig. 4 C and E). The diaphragm offers an additional option. Data indicate larger voltage response for the bovine (Fig. 4F) than the ovine, as shown in Fig. 4 G and H, respectively. Collectively, these results indicate that flexible PZT MEH systems are readily capable of harnessing energy from different locations across the body, with operational details that depend on the species and the organ.

Any long-term practical use would, of course, require efficient operation upon closure of the chest postthoracotomy. Data collected with the chest open (Fig. 5A) and closed (Fig. 5B) show the same capabilities in power generation, as in Fig. 5 C and D. Similar in vivo tests on a pig model appear in *SI Appendix*, Fig. S13. Such results clearly suggest an ability to power implanted devices. The magnitude of power generation in this context is important. Operation of a cardiac pacemaker system provides a specific example of interest. State-of-the-art devices offer cardiac activity sensing, adaptive pacing, and programmability, with average power consumption values as low as $0.3 \mu\text{W}$ (28, 29). The power

Fig. 5. Performance of a PZT MEH evaluated with the chest open and closed and scaling of power output in multilayer stacked designs. Photograph of a PZT MEH without and with battery, rectifier, and pacemaker connection on a bovine heart when the chest is (A) open and (B) closed. Voltage as a function of time for a PZT MEH on the bovine RV with the chest open (C) and closed (D). (E) Schematic illustration of a multilayer stack of five independent PZT MEHs connected in series. A circuit schematic appears in the upper right-hand corner. (F) Photograph of such a stacked configuration, peeled apart at the left edge to show the separate layers. Each device appears just before stacking (*Inset*). (G) Schematic illustration of the theoretical shape for buckling of a stack of PZT MEHs with spin-cast layers of silicone elastomer (thickness = $10 \mu\text{m}$) in-between and under compression. (H) Time-averaged power density as a function of the bending load displacement for stacks consisting of one (pink curve), three (green curve) and five (blue curve) PZT MEHs, connected in series. E, experimental data; T, theory.



output of a PZT MEH depends on its design. With layouts described previously, the time-averaged power density (electrical power output per unit area of PZT) corresponds to 0.12 and 0.18 $\mu\text{W}/\text{cm}^2$ for mounting on the RV at 0° and 45° as seen in *SI Appendix*, Fig. S14 A and B, respectively. Stacking multiple PZT MEH sheets (Fig. 5 E and F and *SI Appendix*, Fig. S15) increases the power output. Fig. 5G shows a stack of n_{MEH} PZT MEHs thin, spin casted of silicone layer in between as adhesives and strain isolating layers. The silicone, which is much more compliant (Young's modulus 60 KPa) than the PI (Young's modulus 2.5 GPa), does not significantly alter the modes of deformation of the PZT MEHs (*SI Appendix*, Table 1). As a result, for a stack of n_{MEH} PZT MEHs, Eq. 5 can be applied simply by replacing N with $N \cdot n_{\text{MEH}}$. For $\Delta L_{\text{max}} = 10$ mm, in multilayer stacks with $n_{\text{MEH}} = 3$ and 5, in vitro experiments show peak voltages of 5.8 and 8.1 V (*SI Appendix*, Fig. S16), respectively, consistent with Eq. 5. Both values are higher than that (3.7 V) for a single-layer device. In vivo demonstrations on the bovine heart are consistent with these results (*SI Appendix*, Fig. S17). The time-averaged power density increases with n_{MEH} , and can reach as large as 1.2 $\mu\text{W}/\text{cm}^2$ (Fig. 5H) for $n_{\text{MEH}} = 5$, which is sufficient to operate a cardiac pacemaker (1) (see *SI Appendix* for details).

Conclusions

The reported results provide evidence that piezoelectric MEHs can yield significant electrical power from motions of internal organs, up to and exceeding levels relevant for practical use in implants. Theoretical models establish design rules and provide predictive capabilities for efficiencies associated with various

single and multilayer layouts. Practical applications demand long-term reliable operation in the closed body cavity. The extensive cycling tests and initial measurements of biocompatibility summarized here represent starting points for the sort of qualifications that are required. In addition to uses on internal organs, the same types of systems can be implemented in skin-mounted configurations for health/wellness monitors or nonbiomedical devices. The potential to eliminate batteries or, at least, the need to replace them frequently represents a source of motivation for continued work in these and related directions.

Materials and Methods

Detailed fabrication steps for the devices, designs for the data acquisition systems, and related hardware all appear in *SI Appendix*. In vitro biocompatibility study and in vivo implantation of the device on animal models are also described in the *SI Appendix*. All animal procedures and experiments were approved by the Institutional Animal Care and Use Committee at the University of Arizona.

ACKNOWLEDGMENTS. We thank Ala'a Al-Okaily for implementation and testing of the mechanical bending stage and the entire clinical team at the University of Arizona Animal Care Facility for their support in animal studies. C.D. thanks M. Dagdeviren for useful suggestions in device design. Research was supported by the US Department of Energy, Office of Basic Energy Sciences, Division of Materials Sciences and Engineering under Award DE-FG02-07ER46471 through the Frederick Seitz Materials Research Laboratory at the University of Illinois at Urbana-Champaign. Y.H. acknowledges Institute for Sustainability and Energy at Northwestern (Northwestern University) for the support of the mechanics modeling effort. M.J.S. acknowledges Prof. D. Bluestein and Grant U01EB012487 from the National Institute of Biomedical Imaging and Bioengineering.

- Karami MA, Inman DJ (2012) Powering pacemakers from heartbeat vibrations using linear and nonlinear energy harvesters. *Appl Phys Lett* 100(4):042901.
- Starner T (1996) Human-powered wearable computing. *IBM Syst J* 35(3.4):618–629.
- Halámková L, et al. (2012) Implanted biofuel cell operating in a living snail. *J Am Chem Soc* 134(11):5040–5043.
- Mercier PP, Lysaght AC, Bandyopadhyay S, Chandrakasan AP, Stankovic KM (2012) Energy extraction from the biologic battery in the inner ear. *Nat Biotechnol* 30(12):1240–1243.
- Wong LS, et al. (2004) A very low-power CMOS mixed-signal IC for implantable pacemaker applications. *IEEE J Solid-State Circuits* 39(12):2446–2456.
- Platt SR, Farritor S, Garvin K, Haider H (2005) The use of piezoelectric ceramics for electric power generation within orthopedic implants. *IEEE/ASME Trans Mechatron* 10(4):455–461.
- Zurbuchen A, et al. (2013) Energy harvesting from the beating heart by a mass imbalance oscillation generator. *Ann Biomed Eng* 41(1):131–141.
- Pfenniger A, Jonsson M, Zurbuchen A, Koch VM, Vogel R (2013) Energy harvesting from the cardiovascular system, or how to get a little help from yourself. *Ann Biomed Eng* 41(11):2248–2263.
- Pfenniger A, Obrist D, Stahel A, Koch VM, Vogel R (2013) Energy harvesting through arterial wall deformation: Design considerations for a magneto-hydrodynamic generator. *Med Biol Eng Comput* 51(7):741–755.
- Choi MY, et al. (2009) Mechanically powered transparent flexible charge-generating nanodevices with piezoelectric ZnO nanorods. *Adv Mater* 21(21):2185–2189.
- Chen X, Xu SY, Yao N, Shi Y (2010) 1.6 V nanogenerator for mechanical energy harvesting using PZT nanofibers. *Nano Lett* 10(6):2133–2137.
- Qi Y, McAlpine MC (2010) Nanotechnology-Enabled Flexible and Biocompatible Energy Harvesting. *Energy Environ Sci* 3(11):1275–1285.
- Zhu G, Yang R, Wang S, Wang ZL (2010) Flexible high-output nanogenerator based on lateral ZnO nanowire array. *Nano Lett* 10(8):3151–3155.
- Song J, Wang ZL (2006) Piezoelectric nanogenerator based on zinc oxide nanowire arrays. *Science* 312(5771):242–246.
- Xu S, Wei YG, Liu J, Yang RS, Wang ZL (2008) Integrated multilayer nanogenerator fabricated using paired nanotip-to-nanowire brushes. *Nano Lett* 8(11):4027–4032.
- Park K-I, et al. (2010) Piezoelectric BaTiO₃ thin film nanogenerator on plastic substrates. *Nano Lett* 10(12):4939–4943.
- Qi Y, et al. (2011) Enhanced piezoelectricity and stretchability in energy harvesting devices fabricated from buckled PZT ribbons. *Nano Lett* 11(3):1331–1336.
- Park SB, Sun CT (1995) Effect of electric-field on fracture of piezoelectric ceramics. *Int J Fract* 70(3):203–216.
- Dagdeviren C, et al. (2013) Transient, biocompatible electronics and energy harvesters based on ZnO. *Small* 9(20):3398–3404.
- Thai HM, et al. (2009) Implantation of a three-dimensional fibroblast matrix improves left ventricular function and blood flow after acute myocardial infarction. *Cell Transplant* 18(3):283–295.
- Hurst JW, Anderson RH, Becker AE, Wilcox BR (1998) *Atlas of the Heart* (Gower Medical, New York).
- Fritz J, et al. (2005) Right ventricle shape and contraction patterns and relation to magnetic resonance imaging findings. *J Comput Assist Tomogr* 29(6):725–733.
- Anzola J (1956) Right ventricular contraction. *Am J Physiol* 184(3):567–571.
- Baciewicz FA, Penney DG, Marinelli WA, Marinelli R (1991) Torsional ventricular motion and rotary blood flow. *Cardiac Chronicle* 5(8):1–8.
- Rushmer RF (1955) Length-circumference relations of the left ventricle. *Circ Res* 3(6):639–644.
- McHale PA, Greenfield JC, Jr. (1973) Evaluation of several geometric models for estimation of left ventricular circumferential wall stress. *Circ Res* 33(3):303–312.
- Streeter DD, Jr., Hanna WT (1973) Engineering mechanics for successive states in canine left ventricular myocardium. I. Cavity and wall geometry. *Circ Res* 33(6):639–655.
- Silveira F, Flandre D (2004) *Low Power Analog CMOS for Cardiac Pacemakers: Design and Optimization in Bulk and SOI Technologies* (Kluwer Academic Publishers, Norwell, MA).
- Ohm OJ, Danilovic D (1997) Improvements in pacemaker energy consumption and functional capability: Four decades of progress. *Pacing Clin Electrophysiol* 20(1):2–9.

Conformal Piezoelectric Energy Harvesting and Storage From Motions of the Heart, Lung and Diaphragm

Canan Dagdeviren^{a,1}, Byung Duk Yang^{a,1}, Yewang Su^{b,c,1}, Phat Le Tran^d, Pauline Joe^a, Eric Anderson^a, Jing Xia^{b,c}, Vijay Doraiswamy^d, Behrooz Dehdashti^e, Xue Feng^f, Bingwei Lu^b, Robert Poston^e, Zain Khalpey^e, Roozbeh Ghaffari^g, Yonggang Huang^c, Marvin J. Slepian^{d,h}, John A. Rogers^{a,i,2}

^a*Department of Materials Science and Engineering, Beckman Institute for Advanced Science and Technology, and Frederick Seitz Materials Research Laboratory, University of Illinois at Urbana-Champaign, Urbana, IL 61801*

^b*Center for Mechanics and Materials, Tsinghua University, Beijing 100084, China*

^c*Department of Civil and Environmental Engineering, Department of Mechanical Engineering, Center for Engineering and Health and Skin Disease Research Center, Northwestern University, Evanston, IL 60208*

^d*Department of Medicine & Sarver Heart Center, The University of Arizona, Tucson, AZ 85724*

^e*Department of Surgery, The University of Arizona, Tucson, AZ 85724*

^f*Department of Engineering Mechanics, Tsinghua University, Beijing 100084, China*

^g*MC10 Inc., Cambridge, MA 02140*

^h*Department of BioMedical Engineering, The University of Arizona, Tucson, AZ 85724*

ⁱ*Department of Chemistry, Department of Mechanical Science and Engineering and Department of Electrical and Computer Engineering, University of Illinois at Urbana-Champaign, Urbana, IL 61801*

¹C.D., B. D.Y., and Y.S. contributed equally to this work.

²To whom correspondence should be addressed. E-mail: jrogers@illinois.edu

Supporting Information

1. SI Materials and Methods

1.1. Fabrication of Lead Zirconate Titanate (PZT) Ribbons Array and Transferprinting Them on PI

PZT ribbons embedded in capacitor type structures with top and bottom electrodes were fabricated as following. The top electrode was formed by deposition of Au/Cr (200 nm/10 nm) with an electron beam evaporator on the surface of a multilayer stack of $\text{Pb}(\text{Zr}_{0.52}\text{Ti}_{0.48})\text{O}_3/\text{Pt}/\text{Ti}/\text{SiO}_2$ (500 nm/300 nm/20 nm/600 nm; INOSTEK) on a silicon wafer. Coating the wafer with photoresist (PR, AZ5214E) followed by patterning by photolithography defines the top electrode areas ($50\ \mu\text{m} \times 2\ \text{mm}$) for each PZT ribbon. Au and Cr layers were etched with gold etchant (TFA, Transene Company Inc., USA) and CR-7 chrome etchant (OM Group, USA), respectively. PZT ribbons with thickness of 500 nm and an area of $100\ \mu\text{m} \times 2.02\ \text{mm}$ were created by wet chemical etching with HNO_3 (nitric acid): BHF (buffered hydrogen fluoride): H_2O (DI water) = 4.51:4.55:90.95 through a hard-baked mask of PR (AZ4620, Clariant) (See Fig. S1A). The hard baking involved $80\ ^\circ\text{C}$ for 5 minutes, $110\ ^\circ\text{C}$ for 30 minutes and then $80\ ^\circ\text{C}$ for 5 minutes (See Fig. S1B). The bottom Pt/Ti electrode with area of $140\ \mu\text{m} \times 2.02\ \text{mm}$ was patterned by wet chemical etching with HCl (hydrochloric acid) : HNO_3 : DI water = 3:1:4 at $95\ ^\circ\text{C}$ through a hard baked mask of AZ4620. The PZT layers were protected by photolithographically patterned PR during partially removal of the sacrificial layer, SiO_2 with dilute HF (hydrofluoric acid) (DI water: 49% HF = 1:3). Hard baked photoresist mask was completely removed in an acetone bath for 3 hours after etching the SiO_2 .

A PDMS stamp for transfer was fabricated by casting a mixture of PDMS (Sylgard 184, Dow Corning; 10:1 ratio of prepolymer to curing agent) in a plastic petri dish, and curing at

room temperature for 24 hours. Next, the stamp was conformally contacted on the top of the ribbons (See Fig. S1C). The devices were retrieved by peeling the stamp away from the Si wafer and then transfer printed on a film of PI (75 μm , DuPont, USA). This film was formed by spin-coating a layer of poly(pyromellitic dianhydride-co-4,4'-oxydianiline) amic acid solution, to a thickness of 1.2 μm (See Supplementary Fig. S1D). The printed PZT ribbons on the PI were spin-coated with another layer of PI for encapsulation and hard baked at 250 $^{\circ}\text{C}$ in a vacuum oven.

To open contact holes for the top and bottom electrodes, the device on PI was patterned with photoresist (PR, AZ 4620), and developed with diluted AZ@400K developer (AZ Electronic Materials, USA) (deionized water (DI) : 400 K developer = 1:2). The PI was etched in reactive ion etching (RIE, March) to open contact holes. Connection lines were obtained by the deposition of Au/Cr (200 nm/10 nm) using electron beam evaporation. The interconnection lines were spin-coated with another layer of PI for encapsulation and hard baked at 250 $^{\circ}\text{C}$ in a vacuum oven.

1.2. Poling of the PZT thin film and device analysis via mechanical testing

The PZT thin films sandwiched between Ti/Pt (20 nm/300 nm) bottom electrode and Cr/Au (10 nm/200 nm) were poled with an electric field of 100 kV/cm at 150 $^{\circ}\text{C}$ for 2 hours. A semiconductor parameter analyzer (4155C, Agilent) was used to measure the open voltage and short current values of mechanical energy harvester. Figure S15 shows a mechanical bending stage for testing the PZT MEH. The system includes a high precision linear stage (ATS100-150; Aerotech, Inc.; USA), equipped with precision ground ball screw, noncontact rotary encoder with 1000 line/rev, and brushless servomotor to achieve a motion with an accuracy of ± 0.5 μm

and a bidirectional repeatability of $\pm 0.3 \mu\text{m}$ over 150 mm stage motion range. The stage can achieve velocities up to 100 mm/sec with maximum side load of 100 N in horizontal configuration. The stage motion was controlled with a Soloist single axis PWM digital controller (SOLOISTTCP20; Aerotech, Inc.; USA) and USB interface. Additionally, two U-Form Vise grip (TH240k, Grip Engineering Thümler GmbH; Germany) were attached to the stage. Pyramid shape jaws (TH240k-BP, Grip Engineering Thümler GmbH; Germany) were attached to the vices to achieve maximum tensile gripping force of 2.5 kN of the specimen during the test. A LabVIEW (National Instruments Corporation; USA) based program was designed to control the stage to perform the test cycle (Fig. S15).

1.3. *In Vitro* Biocompatibility Assessment of the Flexible PZT MEH

Aortic smooth muscle cells (SMC) were harvested from albino Sprague-Dawley rat (with IACUC approval protocol from the University of Arizona) and subsequently cultured in Dulbecco's Modified Eagle Medium (DMEM) supplemented with 10% (v/v) fetal calf serum, 2% (v/v) of 0.2 M glutamine, 1% (v/v) of antibiotic/antimycotic solution. All cell culture supplements and medium were either purchased at Invitrogen (Grand Island, NY, USA) or BioWhittaker (East Rutherford, NJ, USA). SMCs were then sub-cultivated and cultured in an incubator at 37 °C, 5% CO₂, and 95% relative humidity to passages 2-5 before subjecting to ribbonping (trypsin-EDTA), cell counting, and seeding on the sterilized fibronectin (BD-Biosciences, San Jose, CA, USA) coated PZT MEH.

To prepare for biocompatibility studies, PZT MEH ribbons were cut into 1 cm² coupons to fit in a 24 well culture plate. These coupons were then cleaned using Basic Harrick Plasma (Ithaca, NY, USA) for 10 minutes at 1 torr to increase surface hydrophobicity. Subsequently, coupons were sterilized under UV light for 30 minutes then coated with 150 μL of 1 mg/ml fibronectin

for another 15 minutes. Any excess fibronectin was removed and allowed to dry in the culture hood for another 15 minutes prior to 5×10^4 SMCs cultivation for 1, 3, and 9 days at 37 °C, 5% CO₂, and 95% relative humidity. Medium was changed every 24 hours.

At the given latter endpoints, SMCs were stained using actin cytoskeleton/focal adhesion staining kit (Millipore, MA, USA). Cells were fixed with 4% paraformaldehyde for 15 minutes, then washed and permeated the membrane with 0.05% Triton X for 5 minutes. Cells were washed and blocked with 1% protein standard (fractionated bovine serum albumin) in PBS at pH7.4 and subsequently stained with anti-vinculin for 1 hour at room temperature. Cells were washed and stained with fluorescein isothiocyanate conjugated mouse anti-immunoglobulin G (mIgG-FITC) to label vinculin and tetramethyl rhodamine isothiocyanate (TRITC) conjugated Phalloidin to selectively label F-actin. After washing off all the excess stains, cells were then mounted in vector shield with DAPI and imaged using the Nikon C1Si Laser Scanning Confocal Fluorescence Microscope. SMCs on the PZT MEH exhibit normal morphology where intact cytoskeletal fibers, nucleus, and focal adhesion points are present, suggesting that the surface of PZT MEH is a suitable environment for cell growth.

Scanning electron microscopy (SEM, FEI Inspec S, Thermo, Rockford, IL, USA) was also utilized to physically demonstrate the adherent of cells on PZT MEH ribbons. Briefly, SMCs after 9 days of culture were fixed in 5% Glutaraldehyde in PBS at pH7.4 (100% fixator) then subjected to a graded series of water and ethanol (100% fixator → 3:1 → 1:1 → 1:3 → 100% Distilled water → 3:1 → 1:1 → 1:3 → 100% Ethanol. Samples were soaked for 5 min at each step. Finally, Samples were freeze-fried using critical point drying (CPD, EMS #3100, Hatfield, PA, USA). A more detailed CPD protocol can be found in (1). Subsequently, samples were sputter-coated with gold at about 5-8 nm thick and imaged at 30 kV with aperture spot size of 3.

To evaluate the biocompatibility of the PZT MEH structures, the viability and cytotoxicity of SMC were determined after 9 days of cultivation by utilizing two color fluorescence LIVE/DEAD viability (Invitrogen) assay and Lactate Dehydrogenase (LDH) assay (Thermo, IL, USA), respectively. For LIVE/DEAD assay, SMCs grown on PZT MEH ribbon after 9 days were prepared and stained according to manufacture protocol with the exception that samples were mounted in Flouroschild containing DAPI (Sigma Aldrich, St. Louis, MO, USA). Briefly, the culture medium was aspirated from each of the wells then rinsed three times with 1x PBS, and a working solution (consisting of 5 mL 1x PBS, 10 μ L of 2mM EthD-1, and 2.5 μ L of 4mM Calcein AM) was added to cover each of the samples. The submerged samples were incubated for 30 minutes at 37⁰C. After the incubation period, the working solution was removed, and the samples were rinsed once with 1x PBS, then mounted and immediately imaged with the Nikon C1Si fluorescence microscope. For the LDH cytotoxicity assay, 50 μ L medium from cells grown on fiber surfaces at the latter given endpoints (ie. 1, 3, and 9 days) were mixed with 50 μ L reaction mixture (prepared according to the manufacture recipe) in a 96 wells plate for 30 minutes at room temperature. Stop solution (50 μ L) was added and the plate was read at 490/680nm. Mean percent of healthy cells was reported with standard error of mean. All statistical analysis was performed using Microsoft Excel 2010. TTEST was analyzed using one-tailed distribution and two-sample unequal variance type. Statistical significance of differences between the means was determined using a student's t-test ($p = 0.05$).

1.4. Implantation of the PZT MEH: an *In vivo* Study

All animals received humane care and were handled in accordance with IACUC approval protocol at the University of Arizona Animal Care Center. Male Corriente bovine (n=4, 90-140

kg) and domestic ovine (n=1, 45 kg) were used. Animals fasted for 12 hours without food and 8 hours without water prior to left thoracotomy. Animals were operated off-pump, without cardiopulmonary bypass and survived for two hours post-surgery.

Briefly, animal were restrained with Telazol (2.2 mg/kg Intramuscular (IM) or 4 mg/kg Intravenous (IV)), weighed, and anesthetized with 3-5% Isoflurane induction administered via the facemask. An oral endotracheal tube was then placed. Butorphanol (0.01-0.02 mg/kg) and Xylazine (0.1-0.2 mg/kg) were administered via intramuscular (IM) injection into the hamstring muscle to relieve pain. Animal were clipped, shaved, and prepped for the surgery. Glycopyrrolate was administered at 0.002-0.005 mg/kg Intravenous (IV) when bradycardia is present. Animal was then intubated and anesthesia was further maintained at 0.5-3% Isoflurane and at room temperature throughout the study. An orogastric tube was placed to decompress the rumen. A triple lumen catheter (7-8F) was inserted percutaneously into the right jugular vein for IV line for drip infusion of lactated ringers to maintain hydration and for delivery of drugs. An arterial pressure catheter was placed in the carotid artery and ECG was connected to monitor the animal.

Prior to surgery, Ketamine (3-4 mg/kg) and Midazolam (0.25 mg/kg) were inducted intravenously to relax muscle. Pancuronium Bromide (0.04-0.1 mg/kg, IV) were used to block myoneural junctions. Fentanyl (loading dose of 5 µg/kg and dripping dose of 5 to 10 µg/kg/hr), Lidocaine (loading dose of 2 mg/kg and dripping dose of 2 mg/kg/hr), and Ketamine (loading dose of 2 mg/kg and dripping dose of 2 mg/kg/hr) were infused intravenously in addition to inhalant throughout the operation. Left thoracotomy was performed and cauterized with the electro-surgico knife (Conmed Excalibur Plus, Utica, NY, USA). The fifth left rib was snipped and a retractor was used to expose solid tissues like the heart, lung, and diaphragm. Amiodarone

(loading dose of 50 mg IV bolus and dripping dose of 0.3 to 0.9 mg/kg/hr) was administered to control arrhythmias prior to the manipulation of the heart. PZT MEH was then sutured to solid tissues using 2-0 bladed polypropylene (Ethicon, San Angelo, TX, USA). A cable (ACF; Anisotropic conductive film, 3M Co.) was connected to a voltmeter storage monitor systems. To evaluate the responsiveness of the PZT MEH, temporary pacemaker (Medtronic 5388, Minneapolis, MN, USA) and Dobutamine (5-15 $\mu\text{g}\cdot\text{kg}^{-1}\cdot\text{min}^{-1}$, IV) was used to fluctuate the heart rate. After all initial readings, animal were survived for 2 hours to allow the PZT MEH to recharge the battery. Incision sites were closed using the standard technique. At the termination of the surgery, animal were humanely euthanized with 30 ml of Beuthanasia while still under general anesthesia. The PZT MEH was then removed for detailed examination and reading.

2. Theory

2.1. Mechanics analysis

For the out-of-plane displacement $w = A[1 + \cos(2\pi x_1/L)]/2$ shown in Fig. S6A for plane-strain analysis ($\varepsilon_{22} = 0$), the bending energy in PI is related to the curvature w'' by $(\overline{EI}_{PI}/2)\int (w'')^2 ds$, where the integration is over the PI length, and $\overline{EI}_{PI} = (\overline{E}_{PI}t_{PI}^3)/12$, \overline{E}_{PI} and t_{PI} are the plane-strain bending stiffness, plane-strain modulus, and thickness of PI, respectively. The membrane energy can be obtained following the same approach of Song et al. (2). Minimization of the total energy (sum of bending and membrane energies) gives the amplitude A as

$$A = \frac{2}{\pi} \sqrt{L \cdot \Delta L - \frac{\pi^2 t_{kapton}^2}{3}} \approx \frac{2}{\pi} \sqrt{L \cdot \Delta L}, \quad (S1)$$

where the last approximation holds when the compression of PI ΔL is much larger than its critical value $\pi^2 t_{PI}^2 / (3L)$ to initiate buckling. For a 75 μm -thick and 2.5 cm-long PI, $\pi^2 t_{PI}^2 / (3L) \sim 0.74 \mu\text{m}$ is negligible as compared to compression $\Delta L = 1.5 \sim 10 \text{ mm}$ in the experiments.

The bending moment M in PI is related to the curvature w'' by $M = \overline{EI}_{PI} w''$. For the part of PI covered by the PZT ribbons (Fig. S6B), the local curvature is reduced to M / \overline{EI}_{comp} due to the additional bending stiffness of PZT ribbons, where

$\overline{EI}_{comp} = \sum_{i=1}^n \overline{E}_i t_i \left[t_i^2 / 3 + \left(\sum_{j=1}^i t_j - y_{neutral} \right) \left(\sum_{j=1}^i t_j - y_{neutral} - t_i \right) \right]$ is the effective bending stiffness of

multi-layer structure (Fig. S6B) with PI as the 1st layer ($i=1$) and the summation over all n layers, \overline{E}_i and t_i are the plane-strain modulus and thickness of the i^{th} layer, respectively, and

$y_{neutral} = \left[\sum_{i=1}^n \overline{E}_i t_i \left(2 \sum_{j=1}^i t_j - t_i \right) \right] / \left(2 \sum_{i=1}^n \overline{E}_i t_i \right)$ is the distance from the neutral mechanical plane to

the bottom of 1st (PI) layer. The membrane strain in PZT is the axial strain at the center of PZT ribbons, and is given by

$$\varepsilon_m = \left(\overline{EI}_{PI} / \overline{EI}_{comp} \right) w'' h, \quad (\text{S2})$$

where h is the distance from the center of each PZT ribbon to the neutral mechanical plane of the cross section as shown in Fig. S6B. For the length of PZT ribbons much smaller than that of the

PI, w'' is evaluated at the center $x_1=0$ of PZT ribbons as $w'' = -4\pi \sqrt{\Delta L / L} / L$, which gives the membrane strain as shown in Eq. (1) in the main text. For the structure shown in Fig. S6B,

$\overline{E}_1 = 2.83 \text{ GPa}$ and $t_1 = 75 \mu\text{m}$ for PI, $\overline{E}_2 = 2.83 \text{ GPa}$ and $t_2 = 1.2 \mu\text{m}$ for the PI layer,

$\overline{E}_3 = 129 \text{ GPa}$ and $t_3 = 20 \text{ nm}$ for the Ti layer, $\overline{E}_4 = 196 \text{ GPa}$ and $t_4 = 0.3 \mu\text{m}$ for the Pt layer,

$\bar{E}_5 = 69.2 \text{ GPa}$ and $t_5 = 0.5 \mu\text{m}$ for the PZT layer, $\bar{E}_6 = 292 \text{ GPa}$ and $t_6 = 10 \text{ nm}$ for the Cr layer, $\bar{E}_7 = 96.7 \text{ MPa}$ and $t_7 = 0.2 \mu\text{m}$ for the Au layer, and $\bar{E}_8 = 2.83 \text{ GPa}$ and $t_8 = 1.2 \mu\text{m}$ for the PI layer; these give $\bar{EI}_{PI}/\bar{EI}_{comp} = 0.45$, $y_{neutral} = 52.0 \mu\text{m}$ and $h = (t_1 + t_2 + t_3 + t_4 + t_5/2) - y_{neutral} = 24.7 \mu\text{m}$.

2.2. Piezoelectric analysis

The constitutive model of piezoelectric materials gives the relations among the stress σ_{ij} , strain ε_{ij} , electrical field E_i and electrical displacement D_i as

$$\begin{Bmatrix} \sigma_{11} \\ \sigma_{22} \\ \sigma_{33} \\ \sigma_{23} \\ \sigma_{31} \\ \sigma_{12} \end{Bmatrix} = \begin{Bmatrix} c_{11} & c_{12} & c_{13} & 0 & 0 & 0 \\ c_{12} & c_{11} & c_{13} & 0 & 0 & 0 \\ c_{13} & c_{13} & c_{33} & 0 & 0 & 0 \\ 0 & 0 & 0 & c_{44} & 0 & 0 \\ 0 & 0 & 0 & 0 & c_{44} & 0 \\ 0 & 0 & 0 & 0 & 0 & (c_{11} - c_{12})/2 \end{Bmatrix} \begin{Bmatrix} \varepsilon_{11} \\ \varepsilon_{22} \\ \varepsilon_{33} \\ 2\varepsilon_{23} \\ 2\varepsilon_{31} \\ 2\varepsilon_{12} \end{Bmatrix} - \begin{Bmatrix} 0 & 0 & e_{31} \\ 0 & 0 & e_{31} \\ 0 & 0 & e_{33} \\ 0 & e_{15} & 0 \\ e_{15} & 0 & 0 \\ 0 & 0 & 0 \end{Bmatrix} \begin{Bmatrix} E_1 \\ E_2 \\ E_3 \end{Bmatrix}, \quad (\text{S3})$$

$$\begin{Bmatrix} D_1 \\ D_2 \\ D_3 \end{Bmatrix} = \begin{Bmatrix} 0 & 0 & 0 & 0 & e_{15} & 0 \\ 0 & 0 & 0 & e_{15} & 0 & 0 \\ e_{31} & e_{31} & e_{33} & 0 & 0 & 0 \end{Bmatrix} \begin{Bmatrix} \varepsilon_{11} \\ \varepsilon_{22} \\ \varepsilon_{33} \\ 2\varepsilon_{23} \\ 2\varepsilon_{31} \\ 2\varepsilon_{12} \end{Bmatrix} + \begin{Bmatrix} k_{11} & 0 & 0 \\ 0 & k_{22} & 0 \\ 0 & 0 & k_{33} \end{Bmatrix} \begin{Bmatrix} E_1 \\ E_2 \\ E_3 \end{Bmatrix}. \quad (\text{S4})$$

The plane-strain condition $\varepsilon_{22} = 0$ of PZT ribbons, together with $\sigma_{33} = 0$ from the traction free on the top surface of the structure, gives $D_3 = \bar{e}\varepsilon_{11} + \bar{k}E_3$, where $\bar{e} = e_{31} - (c_{13}/c_{33})e_{33}$ and $\bar{k} = k_{33} + (e_{33}^2/c_{33})$ are the effective piezoelectric constants. The electrical displacement can be further obtained as

$$D_3 = \bar{e} \varepsilon_m + \frac{\bar{k}V}{Nt_{PZT}} \quad (S5)$$

from the charge equation $dD_3/dx_3 = 0$ and the relation $E_3 = -\partial\phi/\partial x_3$ between the electrical field and electrical potential, together with the boundary condition that the voltage difference between the bottom and top of PZT is V/N , where V is total voltage between the two ends of the N groups of PZT ribbons in series, and t_{PZT} is the thickness of PZT ribbons. Eq. (S5) shows that the electrical displacement is linear with the membrane strain of PZT ribbons, and is independent of the bending strain. Therefore the bending strain does not contribute to the voltage and current output of the MEH given in the following.

2.3. Current

The voltage V across the two ends of the N groups of PZT ribbons in series is zero after the PZT ribbons are connected to an ampere meter (Fig. S6C). The electrical displacement in Eq. (S5) then becomes $D_3 = \bar{e} \varepsilon_m$, where ε_m is given in Eq. (1) in the main text. Its rate gives the current $I = -A_{PZT} \dot{D}_3$, or equivalently Eq. (2) in the main text, where $A_{PZT} = m(w_{PZT,1}l_{PZT,1} + w_{PZT,2}l_{PZT,2})$ is total area of PZT ribbons in each group; $m=10$ is the number of PZT ribbons in each group, $w_{PZT,1} = 100 \mu\text{m}$, $w_{PZT,2} = 140 \mu\text{m}$, $l_{PZT,1} = 2 \text{ mm}$ and $l_{PZT,2} = 160 \mu\text{m}$ are the widths and lengths of the two rectangular parts of each PZT ribbon, respectively (Fig. S6B).

2.4. Voltage

For voltage measurement, the voltage V in Eq. (S5) across the two ends of the N groups of PZT ribbons in series is no longer zero after the PZT ribbons are connected to a voltmeter (Fig. S6C). The rate of the displacement in Eq. (S5) gives the current $I = -A_{PZT} \left\{ \bar{e} \dot{\varepsilon}_m + \left[\bar{k} / (Nt_3) \right] \dot{V} \right\}$, which, together with the Ohm's law gives Eq. (4) in the main text.

2.5. Rectifier

For current measurements with the rectifier (Fig. S6D), the resistance across the PZT groups is no longer zero because of the resistance of the rectifier $R_{rectifier}$. Instead it is the same as the voltage measurement shown Fig. S6C except that the resistance of the voltmeter R is replaced by $R_{rectifier}$. After this replacement Eq. (5) still holds, but is taken by its absolute value because of the rectifier (3). The current is then obtained from Ohm's law as

$$I = \frac{1}{R_{rectifier}} \frac{(-\bar{e}) N t_{PZT}}{\bar{k}} e^{-\frac{N t_{PZT}}{A_{PZT} R_{rectifier} \bar{k}} t} \left| \int_0^t \frac{d\varepsilon_m}{dt} e^{\frac{N t_{PZT}}{A_{PZT} R_{rectifier} \bar{k}} t} dt \right|. \quad (S6)$$

For the voltage measurement with the rectifier (Fig. S6D), the resistance R is replaced by $R + R_{rectifier}$. After this replacement Eq. (5) still holds for the voltmeter and rectifier in series, and the voltage on the voltmeter is then obtained by multiplying the factor $R / (R + R_{rectifier})$ of the absolute value of Eq. (5) as

$$V = \frac{R}{R + R_{rectifier}} \frac{(-\bar{e}) N t_{PZT}}{\bar{k}} e^{-\frac{N t_{PZT}}{A_{PZT} (R + R_{rectifier}) \bar{k}} t} \left| \int_0^t \frac{d\varepsilon_m}{dt} e^{\frac{N t_{PZT}}{A_{PZT} (R + R_{rectifier}) \bar{k}} t} dt \right|. \quad (S7)$$

2.6. Direction of bending

Figs. S3 and S4 show the strain in PZT bent along x_1 and x_2 directions, respectively, for the axial compression of $\Delta L = 1.5, 3, 5$ and 10 mm. For the same axial compression ΔL , the strain in PZT bent along x_1 direction is larger than that along x_2 direction, and is therefore more effective for energy harvesting.

2.7. The time-averaged power density

The electrical energy output is obtained by integrating the ratio of the square of the voltage V and the resistance R over total time t_{total} as $W = \int_0^{t_{total}} V^2/R dt$ (4). The time-averaged power density is given by $P = W/(t_{total}NA_{PZT})$.

2.8. FEA for the deformation of the stacks

Finite element analysis (FEA) is used to study the deformation of a single PZT MEH and the stacks of 3 and 5 PZT MEHs with spin-casted silicone layer of $10 \mu\text{m}$ thickness in between. The solid elements in the ABAQUS finite element program (5) are used to mesh all materials, including the PZT ribbons. Fig. S18 shows that the amplitudes of the PZT MEHs in the stacks are very close to that of the single PZT MEH, with the difference less than 1%, which clearly suggests that the soft silicone layers do not make significant contribution to the deformation of the PZT MEHs.

References

1. Thomasson SA, Thomasson JR (2011) A comparison of CPD (critical point drying) and HMDS (hexamethyldisilazane) in the preparation of *Corallorhiza* spp. rhizomes and associated mycorrhizae for SEM (scanning electron microscopy). *Transactions of the Kansas Academy of Science* 114(1&2):129-134.
2. Song J, et al. (2009) Mechanics of noncoplanar mesh design for stretchable electronics circuits. *Journal of Applied Physics* 105(12):123516.
3. Bishop O (2011) *Electronics A First Course*. Elsevier Ltd., Burlington, MA.
4. Andosca R, et al. (2012) Experimental and theoretical studies on MEMS piezoelectric vibrational energy harvester with mass loading. *Sensors and Actuators A* 178:76-87.
5. Dassault Systèmes (2010) Abaqus analysis user's manual v.6.10. Dassault Systèmes Simulia Corp., Providence, RI.

SI Figure Legends

Figure S1. Schematic illustration of procedures for fabricating a PZT MEH on a polyimide (PI) substrate. Schematic illustration of (A) array of ribbons of PZT in a capacitor structure on a SiO₂/Si wafer (left). A cross section of one element in this array appears on the right. (B) Pattern of photoresist on the array (left), and cross section of one element during undercut etching with dilute HF solution (right). (C) Retrieving the array with a PDMS stamp to leave them adhered to the surface of the stamp. (D) Result after transfer printing onto a flexible film of PI.

Figure S2. Fabrication steps to fabricate PZT ribbons. Optical microscope image of printed ribbons of PZT on a film of PI (A) before bending, (B) after bending with the radius of 20 mm curvature and (C) with the view of top and bottom connection pads. (D) The cross sectional illustration of a ribbon of PZT with top and bottom electrodes, on a PI substrate with a thin overcoat of PI for encapsulation. (E) Schematic illustration of PZT ribbons grouped and connected in series.

Figure S3. Results of FEM analysis for strain mapping of the bare PZT ribbons array. (A) Deformation of a PZT MEH and (B) corresponding strain distributions in the ribbons of PZT. The displacement loads (ΔL) correspond to 0, 1.5, 3, 5 and 10 mm along the x_1 direction, from left to right.

Figure S4. Results of FEM analysis for strain mapping of the bare PZT ribbons array. (A) Deformation of a PZT MEH and (B) corresponding strain distributions in the ribbons of PZT. The displacement loads (ΔL) correspond to 0, 1.5, 3, 5 and 10 mm along the x_2 direction, from top to bottom.

Figure S5. Experimental and theoretical results for displacement, voltage, and current as a function of time for cyclic bending of a PZT MEH with rectification.

Figure S6. Device layouts and information related to variable names and physical parameters used in calculations. Schematic illustration of (A) the theoretical shape for buckling of a PZT MEH under compression, (B) top view of a single PZT ribbon capacitor structure (top), and cross section showing

position of the neutral mechanical plane of the device (bottom). A buckled array of PZT ribbon capacitor structures on a PI substrate without (C) and with (D) rectification.

Figure S7. Images that show the ability of flexible PZT MEHs to conform to various surfaces.

Photograph of a PZT MEH (A) on a balloon. (B) A magnified view of the device. Photograph of a PZT MEH wrapped onto the (C) arm and (D) finger.

Figure S8. Responses of a PZT MEH for forward and reverse connections. (A) Forward and (B)

reverse connections to the measurement system. (C) Open-circuit voltage and (D) short-circuit current of a PZT MEH under cyclic bending for these two configurations.

Figure S9. Studies of cycle life in a PZT MEH. Photographs of device clamped in a bending

stage with a layer of a transparent gelatine (Knox) on top, in (A) flat and (B) bent states. Output voltage as a function of time after a single cycle of bending (C) and twenty million cycles of bending (D).

Figure S10. Output from a PZT MEH mounted on the bovine heart, for different pacing conditions.

Voltage as a function of time measured from a PZT MEH on the (A) RV, (B) LV, and (C) free wall of a bovine heart at 0° with respect to the apex, at heart rates of 80, 90, 100, 110, and 120 beats/min.

Figure S11. Output from a PZT MEH mounted on the ovine heart, for different pacing conditions.

Voltage as a function of time measured from a PZT MEH on the (A) RV, (B) LV, and (C) free wall of a bovine heart at 0° with respect to the apex, at heart rates of 110, 120 and 130 beats/min; respectively.

Figure S12. Output from a PZT MEH mounted on the bovine heart for different levels of

dobutamine infusion. Voltage as a function of time measured from a PZT MEH on the (A) LV, (B) RV of a bovine heart at 0° with respect to the apex with 0, 2, 5, 10 and 15 $\mu\text{g}\cdot\text{kg}^{-1}\cdot\text{min}^{-1}$ of dobutamine.

Figure S13. Performance of a PZT MEH evaluated with the chest open and closed on a pig model.

Photograph of a PZT MEH without battery and rectifier connection on pig heart when the chest is (A) open and (B) closed. Voltage as a function of time for a PZT MEH on the pig LV with the chest open (C) and closed (D).

Figure S14. Effect of orientation of the PZT MEH with respect to the apex of a bovine heart.

Voltage as a function of time measured on the RV of a bovine heart with 80 beats/min (A) at 0° and (B) at 45° .

Figure S15. Image of the experimental setup used for bending and cycling tests. (A) The picture here

shows testing of a five layer stack of PZT MEHs, with a LabVIEW control interface. A cross sectional image of the stacked device appears in the top left. (B) A photograph of LabVIEW controllable mechanical bending stage.

Figure S16. Output voltage as a function of time measured from a stacked arrangement of PZT MEHs. Experimental and theoretical results for displacement, voltage as a function of time, for four different bending load displacements. Spin-cast layers of silicone bond the separate PZT MEHs.

Figure S17. *In vivo* evaluation of stacked PZT MEHs on voltage output. Voltage as a function of time for devices that incorporate (A) 3 and (B) 5 layers of PZT MEHs connected in series and mounted in the RV of a bovine heart (80 beats/min) at 0° (left) and at 45° (right).

Figure S18. The buckle amplitude of a single PZT MEH and that of each PZT MEH in the stacks, incorporating 3 and 5 PZT MEHs with spin-casted silicone layer of 10 μm thickness in between, for compression $\Delta L = 5$ mm. The differences between the amplitudes are very small, which suggests that the soft silicone layers do not make significant contribution to the deformation of the PZT MEHs.

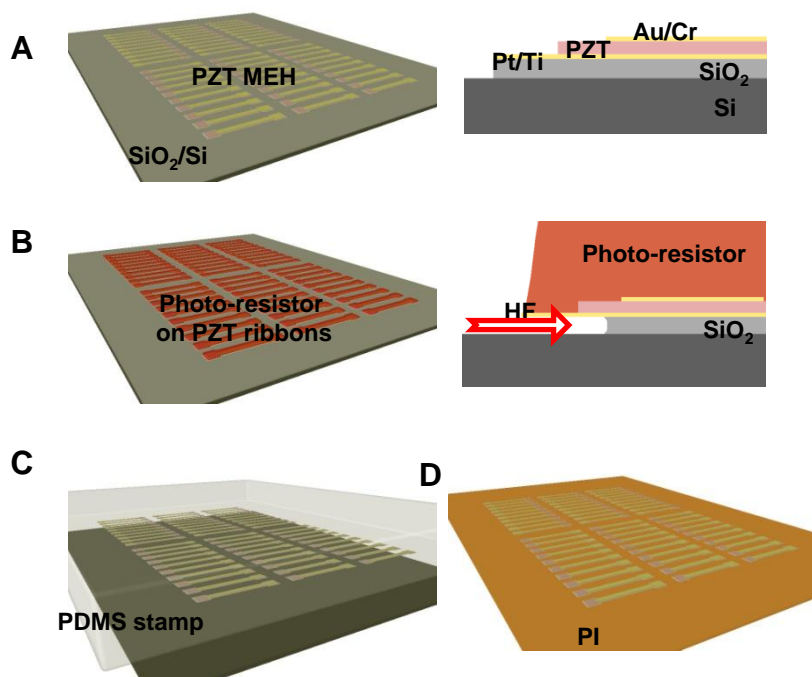


Figure S1

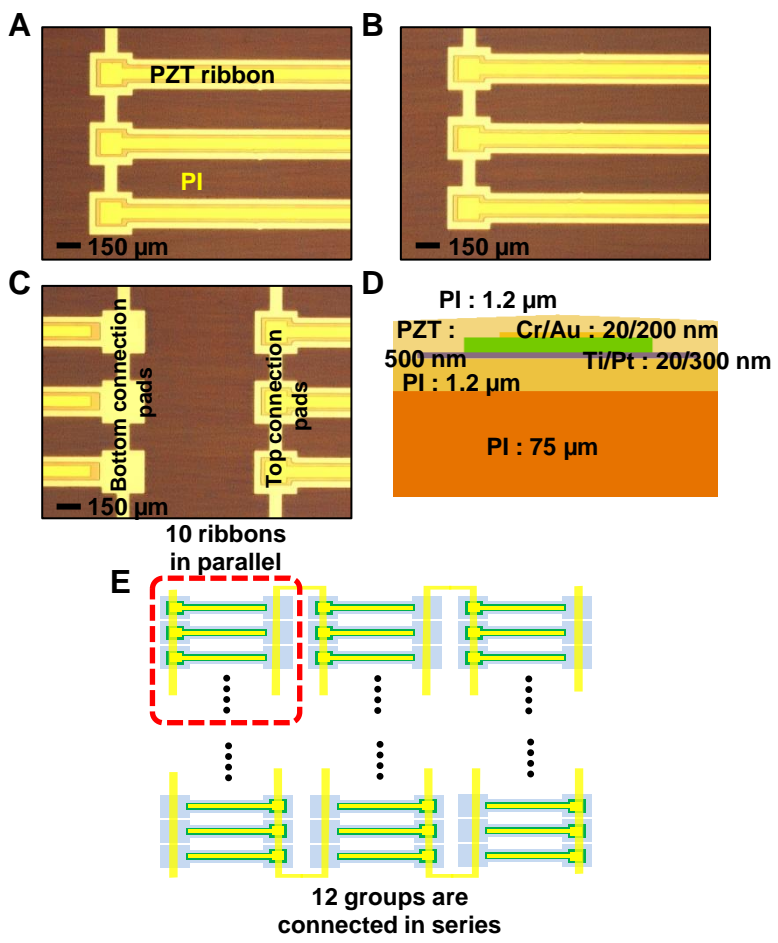


Figure S2

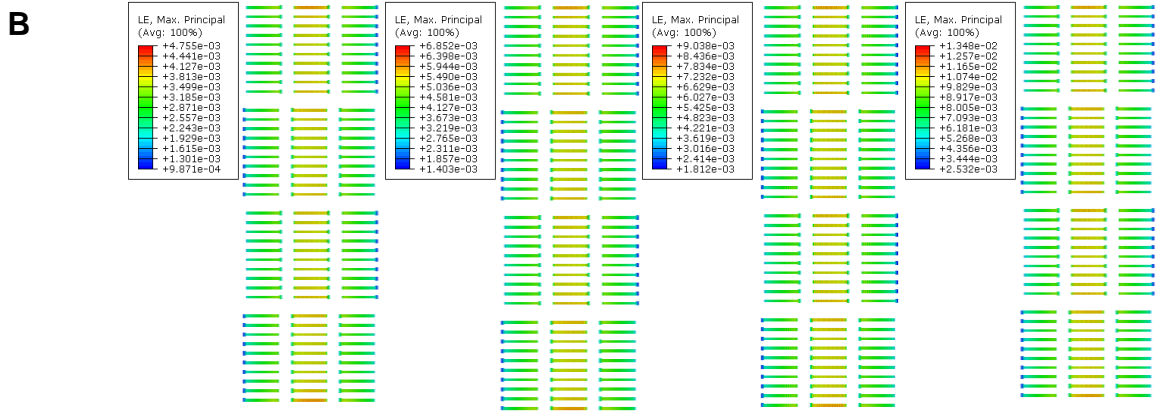
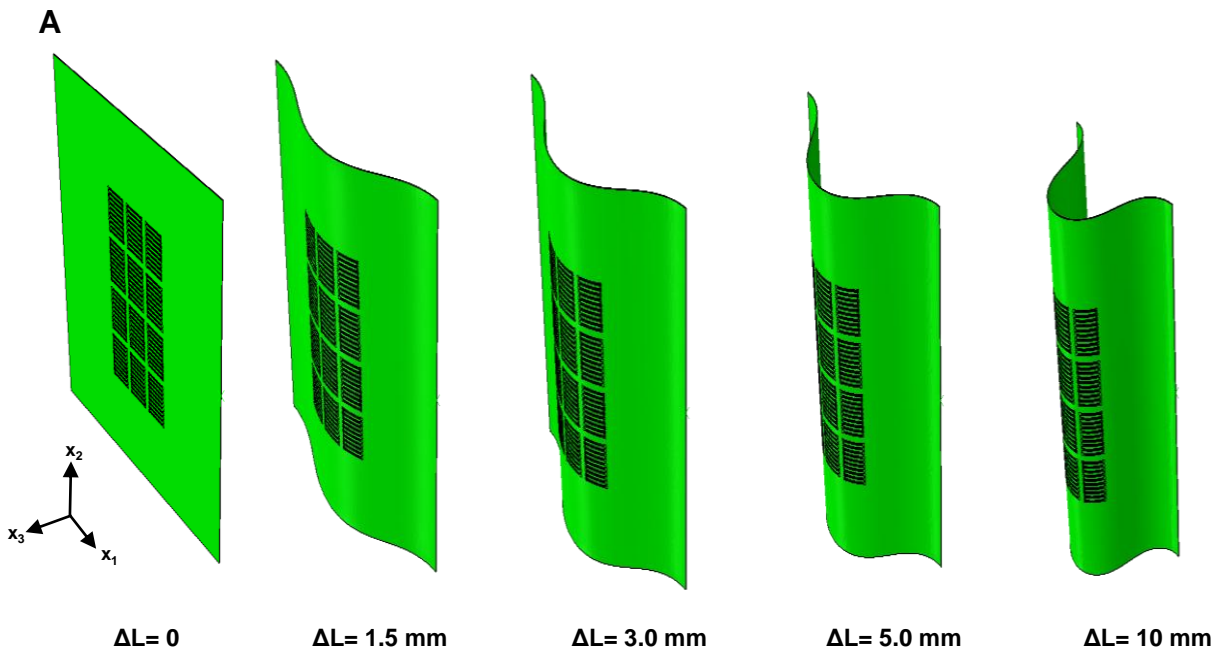


Figure S3

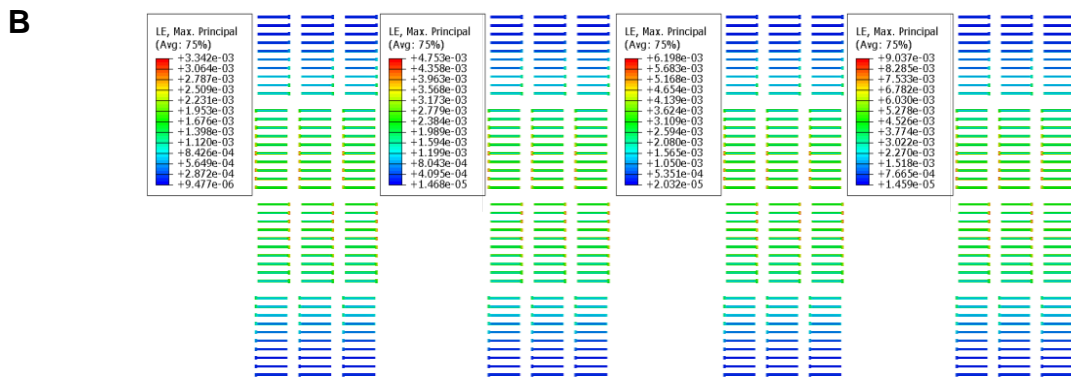
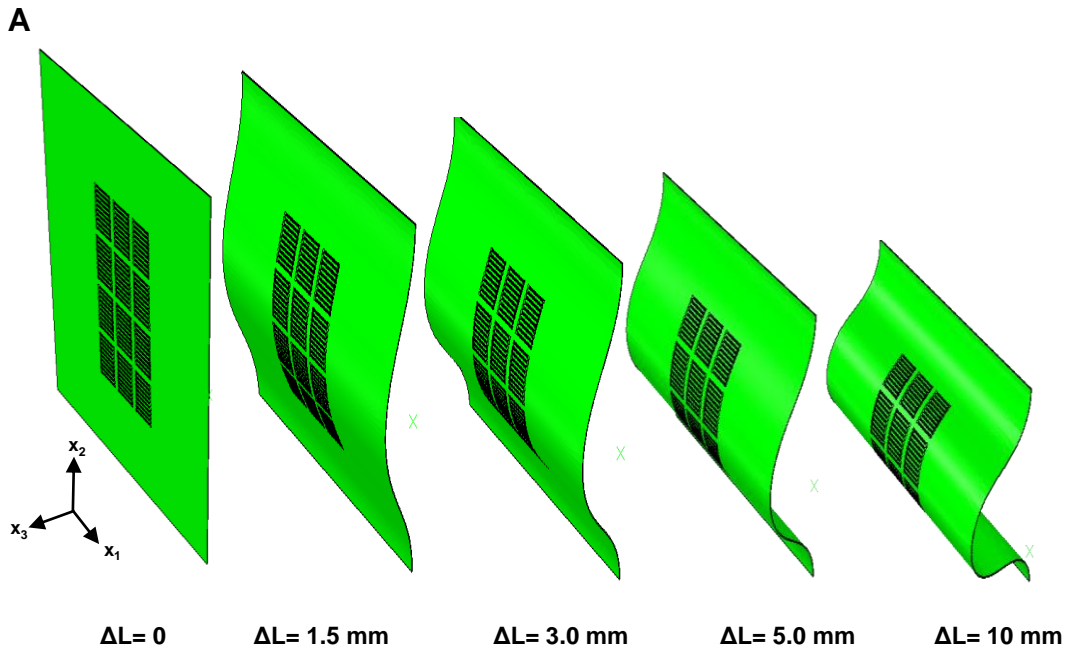


Figure S4

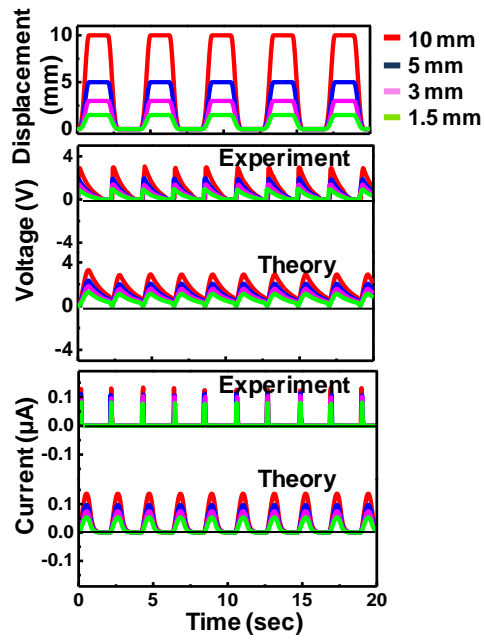


Figure S5

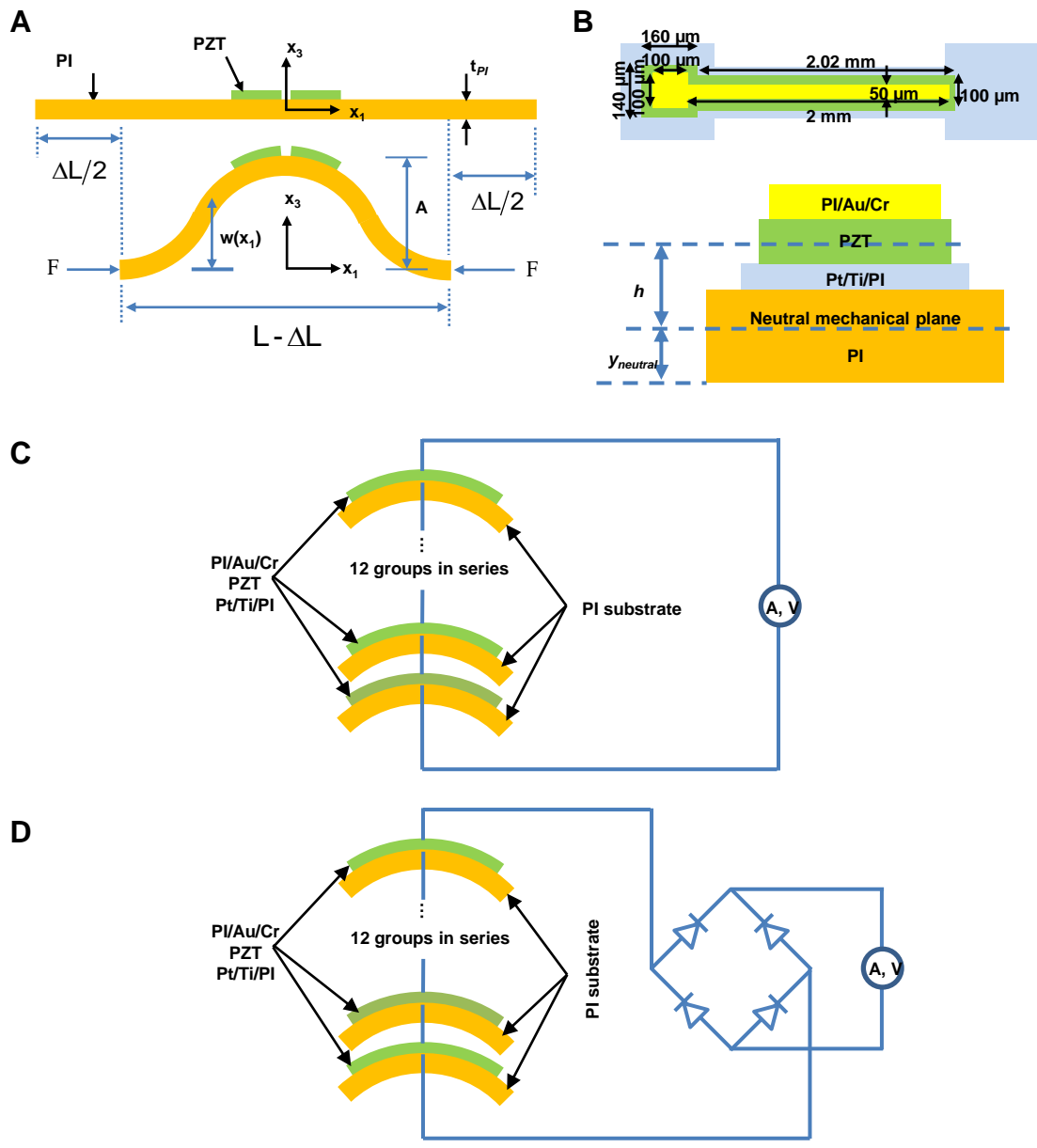


Figure S6

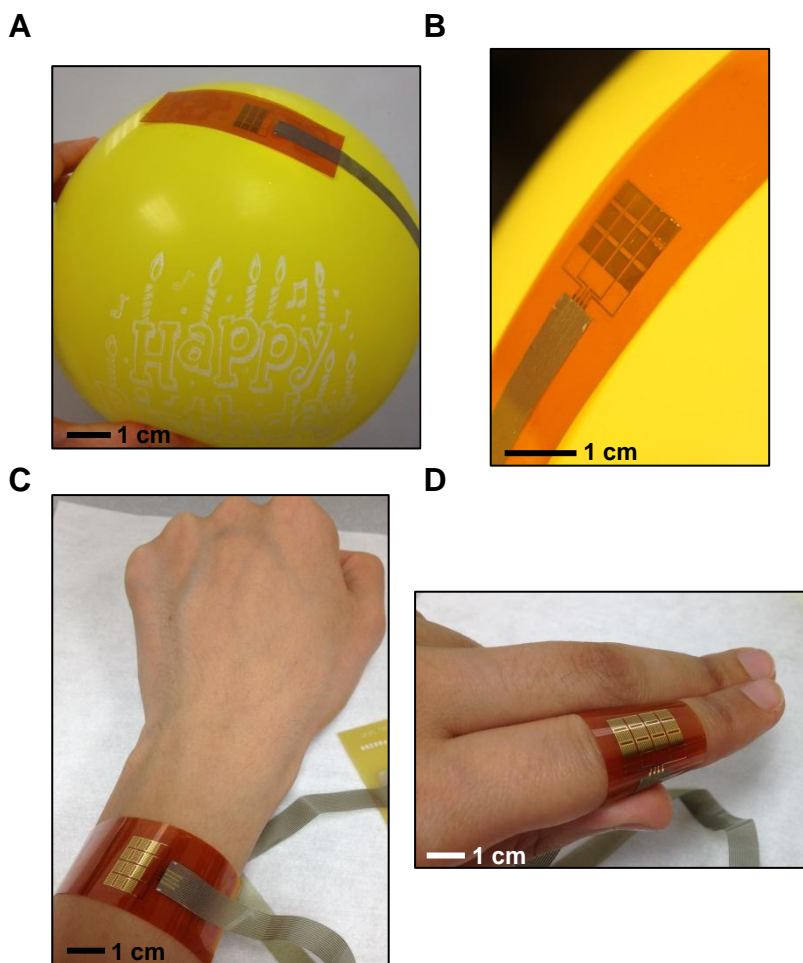


Figure S7

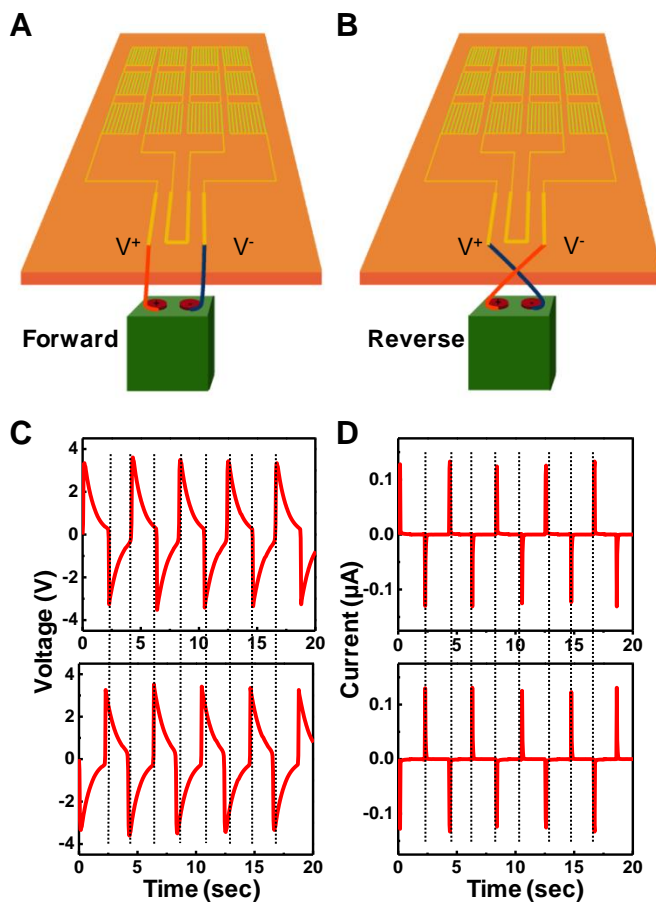


Figure S8

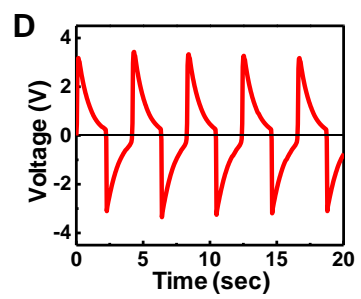
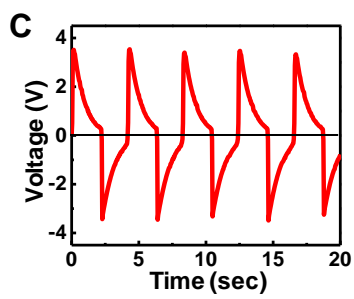
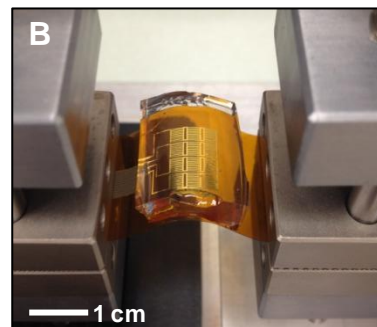
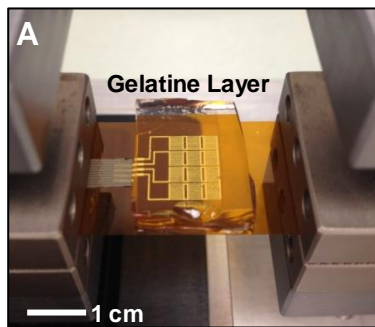


Figure S9

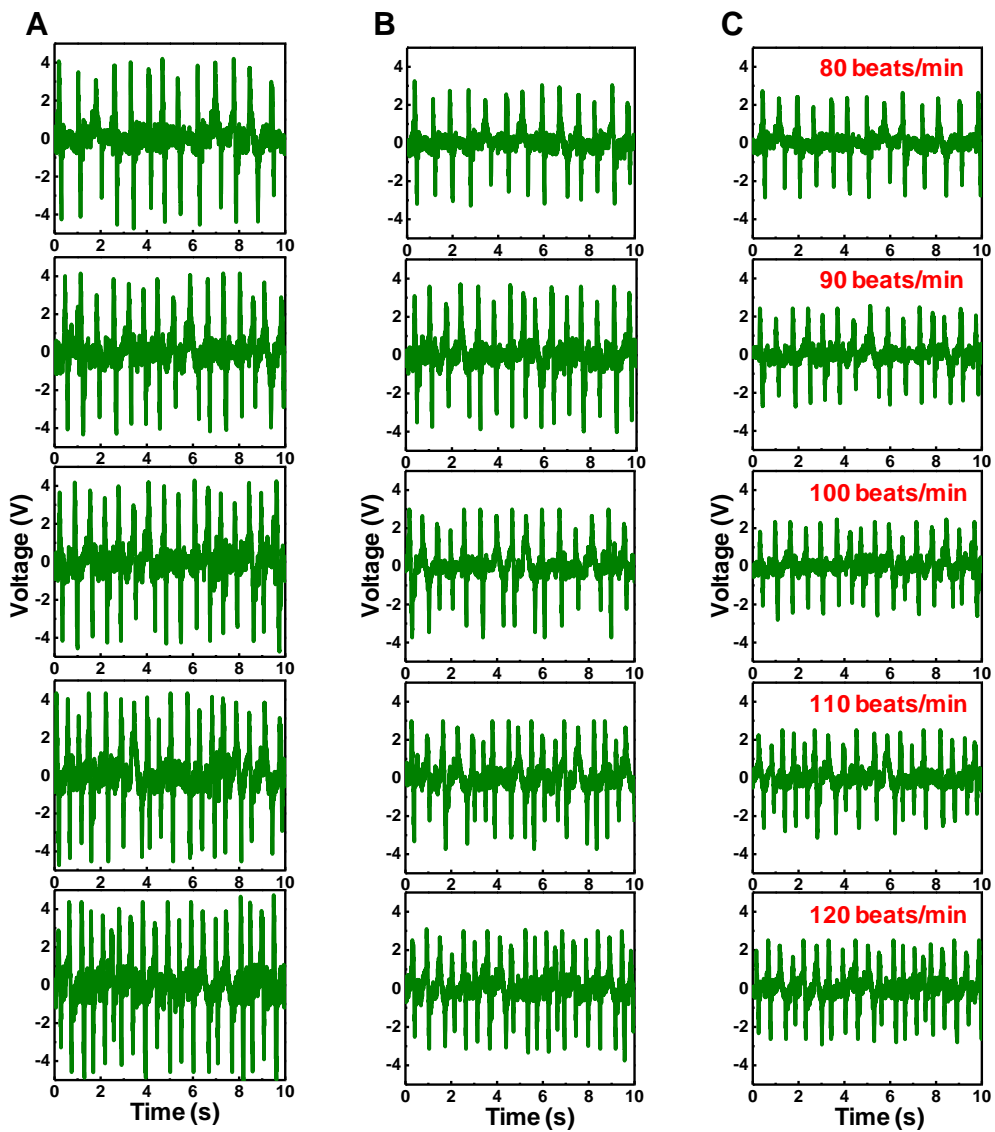


Figure S10

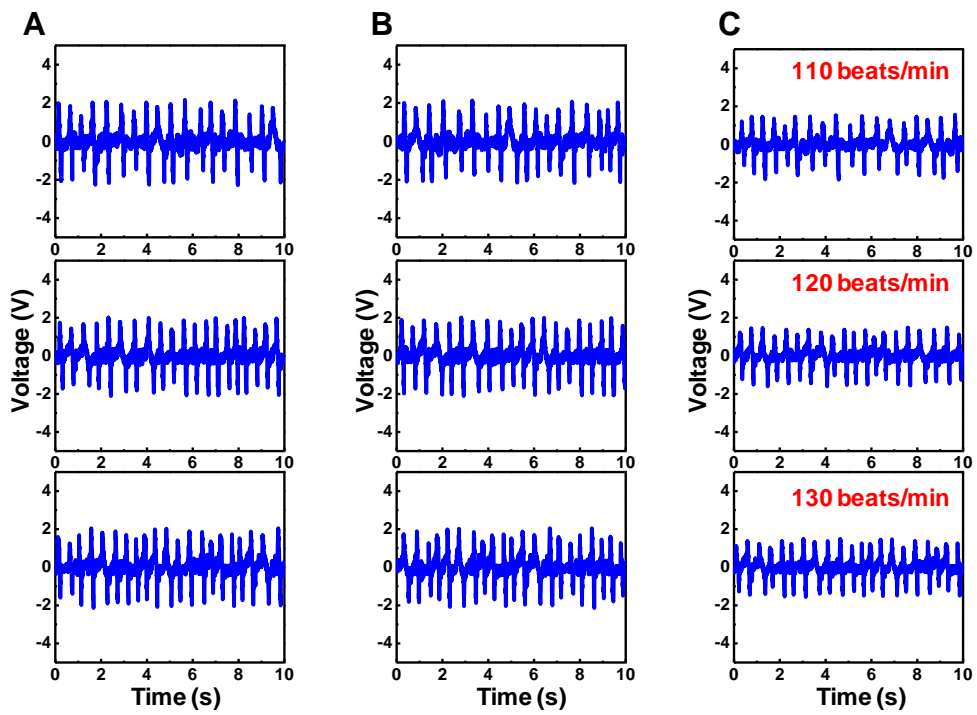
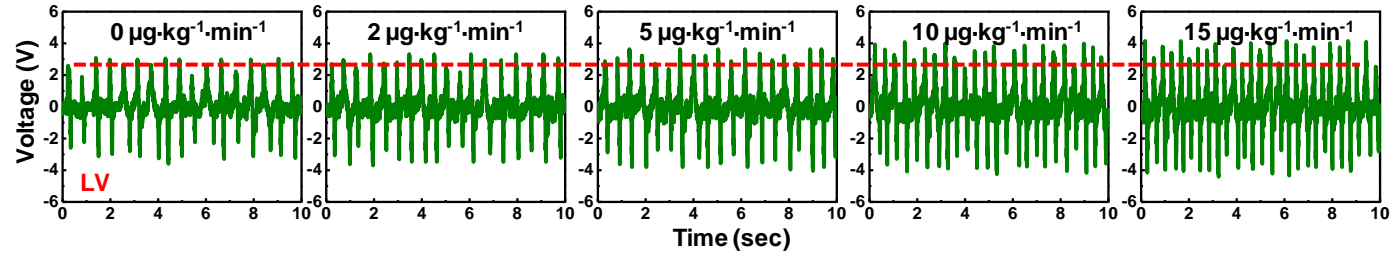
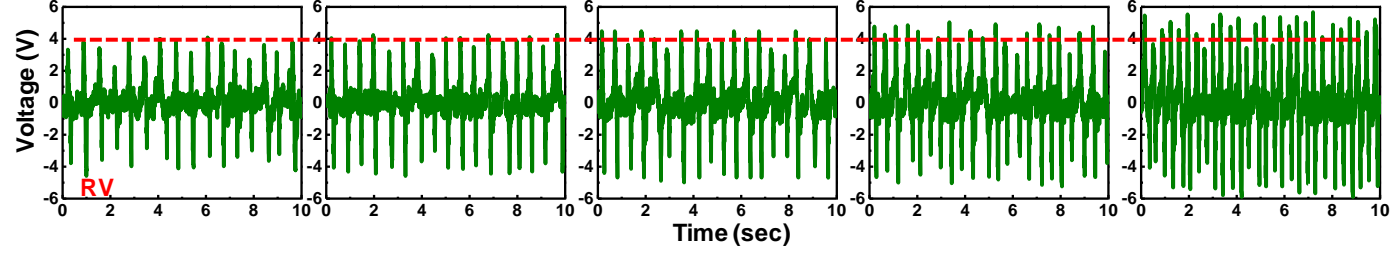


Figure S11

A**B****Figure S12**

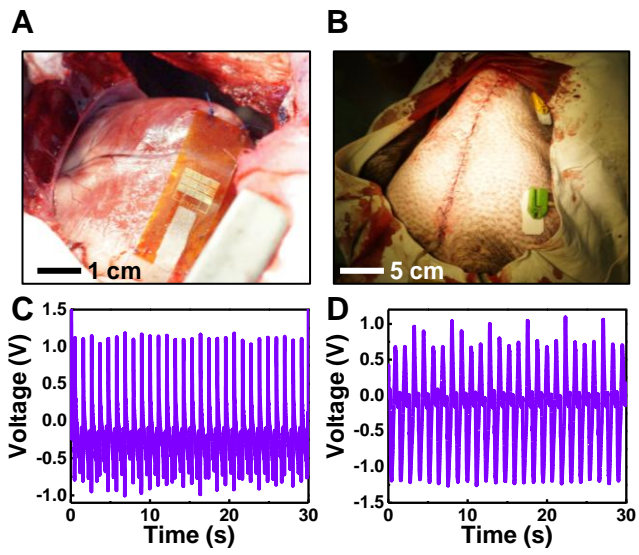


Figure S13

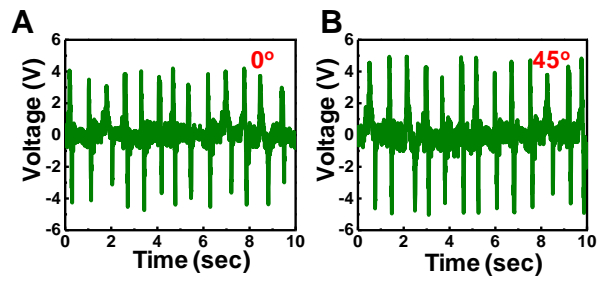
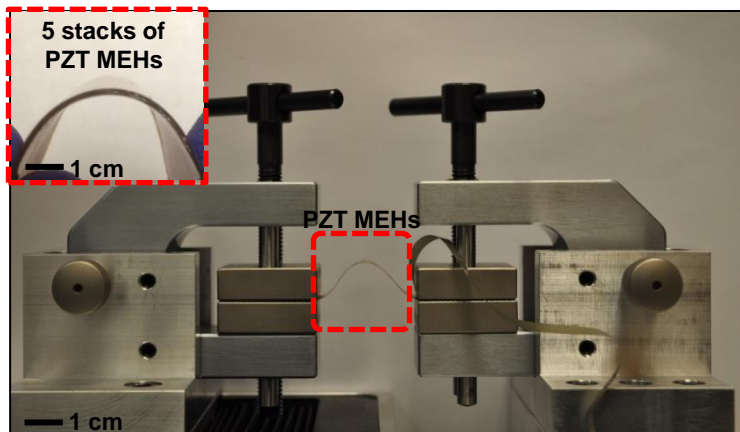


Figure S14

A



B

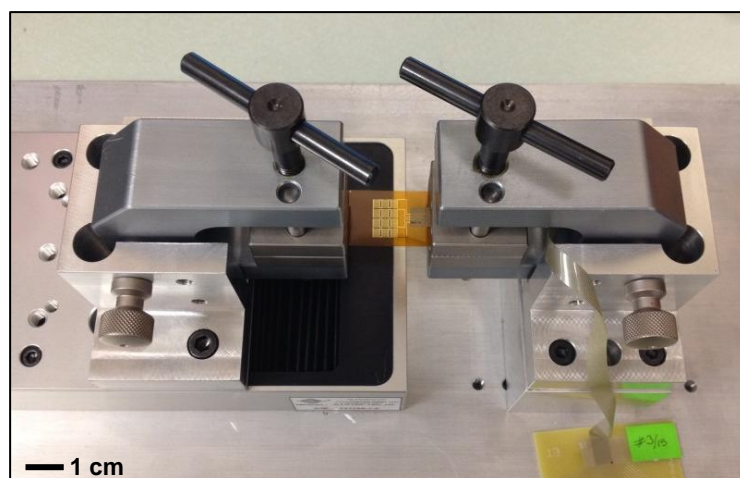


Figure S15

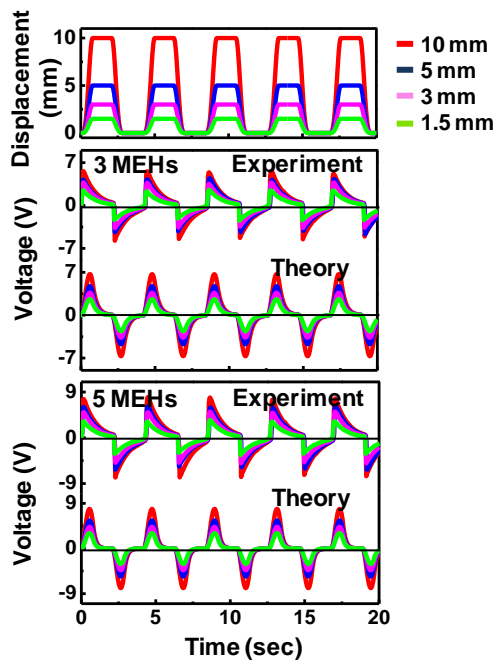


Figure S16

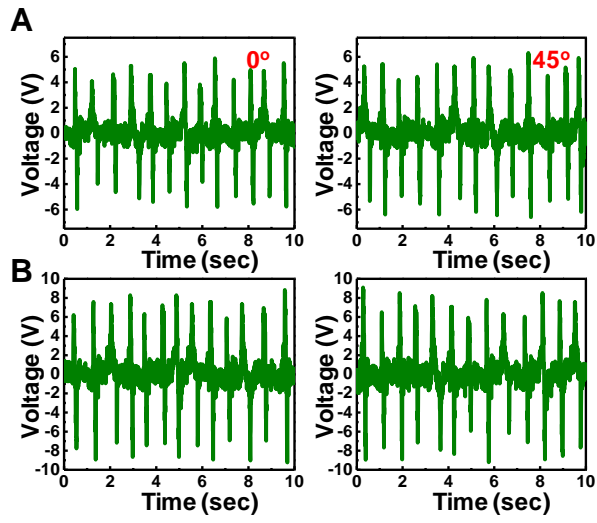


Figure S17

Table 1 The amplitude of the stacks for $\Delta L=5$ mm.

	n th PZT MEH	Amplitude (mm)
single PZT MEH	1	6.41
	3	6.37
stack of 3 PZT MEHs	2	6.37
	1	6.37
	5	6.35
stack of 5 PZT MEHs	4	6.35
	3	6.35
	2	6.35
	1	6.35

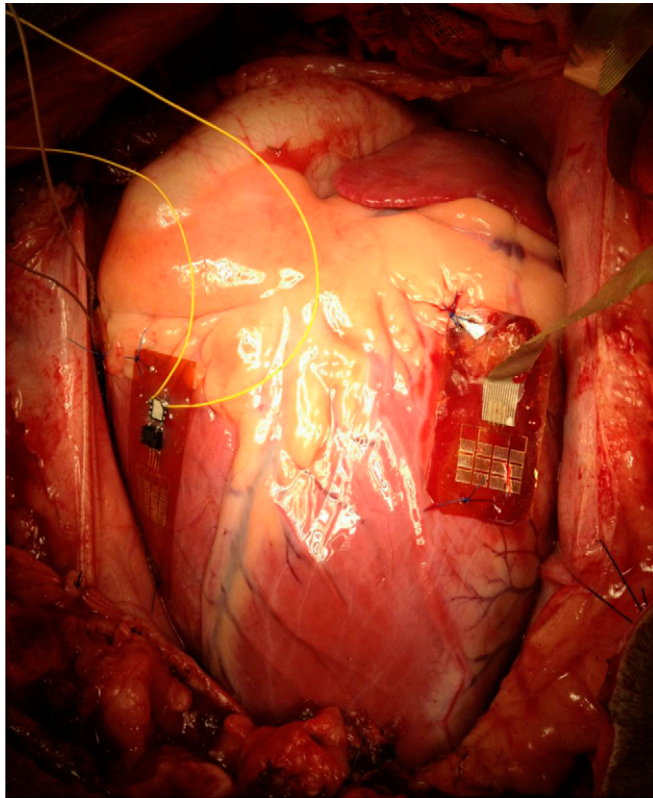
Supporting Information

Dagdeviren et al. 10.1073/pnas.1317233111



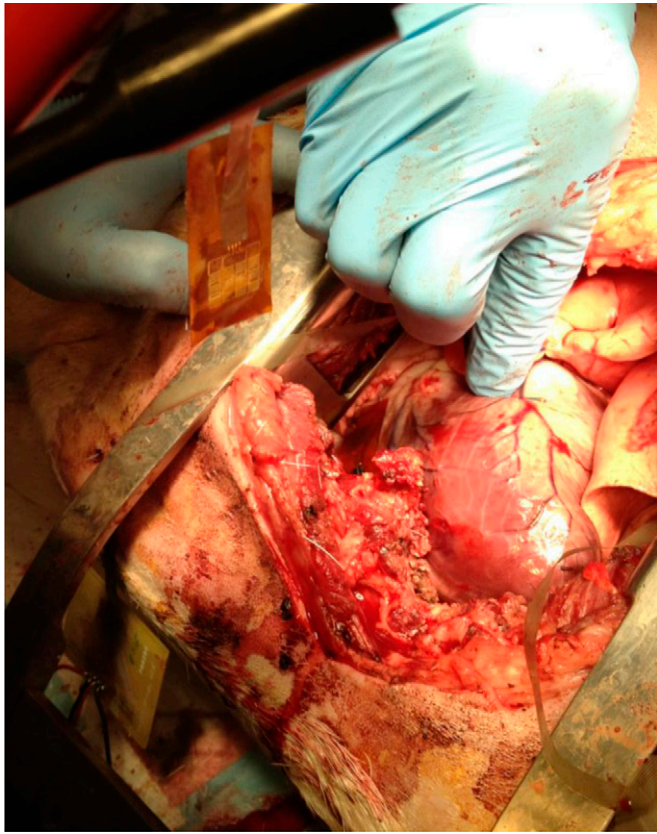
Movie S1. Affixing procedure of lead zirconate titanate (PZT) mechanical energy harvester (MEH) on epicardial sites. The anchoring scheme used sutures at three points, to maintain focal contact, though without rigid attachment so as to minimize any alteration or constraint on cardiac motion.

[Movie S1](#)



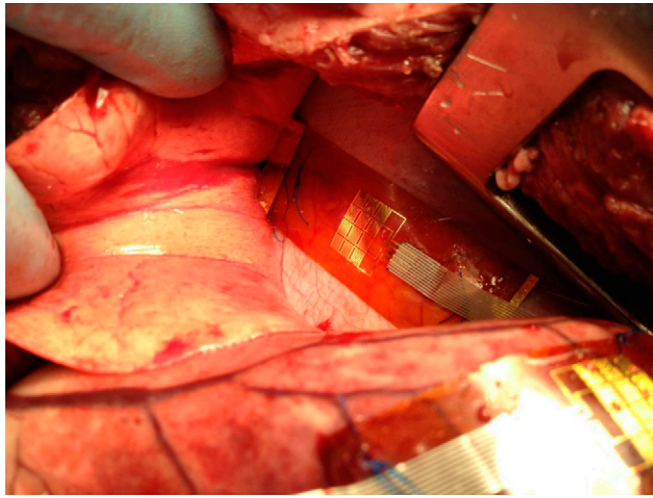
Movie S2. PZT MEH on the left and right ventricles of the bovine heart.

[Movie S2](#)



Movie S3. Increasing heart rate with a temporary pacemaker.

[Movie S3](#)



Movie S4. PZT MEH on the bovine lung.

[Movie S4](#)

Other Supporting Information Files

[SI Appendix \(PDF\)](#)